PHILOSOPHICAL TRANSACTIONS OF THE ROYAL SOCIETY A MATHEMATICAL, PHYSICAL & ENGINEERING SCIENCES

Free and Forced Oscillation of a Vertical Tube Containing a Flowing Fluid

R. E. D. Bishop and I. Fawzy

Phil. Trans. R. Soc. Lond. A 1976 **284**, 1-47
doi: 10.1098/rsta.1976.0098

FREE AND FORCED OSCILLATION OF A VERTICAL TUBE CONTAINING A FLOWING FLUID

By R. E. D. Bishop† and I. Fawzy‡

† *Department of Mechanical Engineering, University College London*

‡ *Department of Mechanical Design, Faculty of Engineering, University of Cairo, Egypt*

(*Communicated by A. R. Collar, F.R.S. – Received 8 November 1974 – Revised 22 September 1975*)

[Plate 1]

CONTENTS

 [Published 21 December 1976

A flexible vertical tube, clamped at its upper end and carrying a nozzle at its free lower end, can become unstable when a liquid flows down it. The system is a convenient one for the study of passage through an instability boundary as it is amenable to theoretical and experimental investigation of both free and forced oscillation. This paper presents the results of a theoretical and experimental study of the motions with special reference to the instability boundary.

1. Introduction

The vibration of a flexible tube conveying fluid is an interesting phenomenon that possesses considerable technological importance. A paper by Ashley & Haviland (1950) was perhaps the first published on the subject. Since its appearance, the subject has been discussed frequently (Paidoussis 1970). By contrast, the harmonic response of dynamical systems near the instability boundary has only been discussed in a few papers. The first study of this kind was perhaps that of Frazer & Jones (1937). Their work dealt principally with a method proposed earlier by von Schlippe (1936) for estimating the critical flutter speed of an aeroplane. A sequel paper appeared later by Frazer (1939). Brann (1965) used a harmonic test to investigate the stability of a rudimentary model railway bogie. In a later paper, Brann (1967) discussed the implications of the harmonic resonance test near the state of instability. Muhlstein (1966) used a forced vibration method based upon the concept of mechanical impedance to investigate panel flutter. Nevertheless it remains true that the literature in this field is sparse.

The studies reported in this paper were conceived as a possible means of investigating a technical problem of extreme importance, namely the flutter of aircraft. It is not suggested, of course, that a vertical tube conveying a liquid bears much resemblance to an aircraft in flight, but such similarities as there are are perhaps worthy of some thought.

To study the phenomena that are normally associated with flutter and flight flutter testing, and to which simple flutter calculations apply, it would evidently be helpful to consider a much simpler system than an aircraft. That system should ideally satisfy a number of requirements:

(*a*) It should be simple with simple mode shapes.
(*b*) It should be easy to take the system through an instability boundary, and preferably more than one.
(*c*) The system should lend itself readily to resonance testing.
(*d*) The system should be essentially a 'linear' one.

The system that is examined here meets all these requirements. Moreover, the system is such that the fluid forces at any instant are accurately determined by the motion at that instant, thus

rendering the simplifying assumption of 'quasi-steady flow' (that is sometimes made in rudimentary aeroelasticity calculations) a tenable one.

1.1. *Notation*

$\boldsymbol{A}$ structural stiffness matrix; see equation (41)
A sectional area of tube
A_n nozzle area
b viscous damping constant
EI flexural rigidity of tube
$\boldsymbol{E}$ fluid (hydrodynamic) damping matrix; see equation (41)
F_0 amplitude of harmonic exciting force
F_x, F_v force per unit length applied to tube by fluid in the direction Ox, Ov
F_z dimensionless amplitude of force applied at section $X = z/l$
f distribution of external force, a function of x; frequency parameter
$\boldsymbol{G}$ fluid stiffness matrix, see equation (41)
$\boldsymbol{H}$ gravity stiffness matrix, see equation (41)
h assumed amplitude of P in forced motion
$\boldsymbol{I}$ unit matrix
l length of tube
m_1 mass/unit length of tube
m_2 mass/unit length of fluid inside the tube
n number of modes admitted, see equation (10)
P dimensionless generalized coordinate
$\boldsymbol{P}$ column matrix of generalized coordinates P
p gauge pressure of fluid
p_l gauge pressure of fluid just above nozzle
p_n gauge pressure exerted by fluid on upper surface of nozzle plate
Q generalized force
q generalized coordinate, see equation (10)
$\boldsymbol{R}$ matrix of dimensionless applied generalized forces
R distributed normal reactive force per unit length, see figure 3 (b); rotameter discharge parameter
$\boldsymbol{T}$ dimensionless time; kinetic energy
T_l tension in tube just above the nozzle
U flow velocity inside the tube
u Assumed complex amplitude of P in forced motion
V dimensionless lateral displacement $= v/l$; potential energy
W work done by lateral external loading; virtual work
w vertical rise of the tube section due to lateral deflexion
X dimensionless distance along tube $= x/l$
x distance along tube from top
Z dimensionless distance of excitation point from top of tube
z distance of point of excitation from top of tube
α nozzle parameter = ratio of fluid speed in the nozzle to fluid speed in the tube
α_{XZ} dimensionless receptance

PHILOSOPHICAL TRANSACTIONS OF THE ROYAL SOCIETY A MATHEMATICAL, PHYSICAL & ENGINEERING SCIENCES

β Mass ratio parameter, see equation (39)
γ weight parameter, see equation (39)
θ slope of the tube with respect to the vertical
ζ dimensionless distributed applied force
η dimensionless measure of viscous damping
κ dimensionless measure of Kelvin damping
λ_s constant appearing in expression for $\phi_s(x)$
μ velocity parameter, see equation (39)
μ_c value of μ at stability boundary
σ dimensionless frequency
σ_c value of σ at stability boundary
ν Kelvin damping constant
Φ dimensionless characteristic function
$\boldsymbol{\Phi}_z$ column matrix of values of Φ for $X = z/l$
ϕ characteristic function of cantilever
ω dimensionless driving frequency
ω_0 frequency of harmonic exciting force

A dot over a symbol signifies a derivative with respect to t or T.
Primes signify derivatives with respect to x or X.

1.2. *General background*

Before going into the details of our system it may be useful to discuss the general problem of forced oscillation of a non-conservative system. In doing so we shall employ a notation that is peculiar to this section; this is the simplest way of avoiding confusion with the symbolism used later on.

A typical system may be represented by the matrix equation

$$\boldsymbol{A}(\mu)\,\ddot{\boldsymbol{q}} + \boldsymbol{B}(\mu)\,\dot{\boldsymbol{q}} + \boldsymbol{C}(\mu)\,\boldsymbol{q} = \boldsymbol{F}\,\mathrm{e}^{\mathrm{i}\omega t}, \tag{1}$$

where $\boldsymbol{A}(\mu)$, $\boldsymbol{B}(\mu)$ and $\boldsymbol{C}(\mu)$ are the inertia, damping and stiffness matrices, μ being a disposable parameter such as air speed in flutter problems or flow velocity in the problem of a flexible tube conveying fluid. $\boldsymbol{F}$ is a column matrix of amplitudes of harmonic excitation (the driving frequency being ω) and $\boldsymbol{q}$ is a vector of generalized coordinates. The matrices $\boldsymbol{A}(\mu)$, $\boldsymbol{B}(\mu)$ and $\boldsymbol{C}(\mu)$ are real and of order $n \times n$, while $\boldsymbol{F}$ and $\boldsymbol{q}$ are of order $n \times 1$.

The steady response of the system may be written as

$$\boldsymbol{q} = \boldsymbol{Q}\,\mathrm{e}^{\mathrm{i}\omega t}, \tag{2}$$

where $\boldsymbol{Q}$ is a complex vector. On substitution of equation (2) into (1) we find that

$$[\boldsymbol{C}(\mu) - \omega^2\boldsymbol{A}(\mu) + \mathrm{i}\omega\boldsymbol{B}(\mu)]\,\boldsymbol{Q} = \boldsymbol{F}, \tag{3}$$

or

$$\boldsymbol{S}(\mu, \mathrm{i}\omega)\,\boldsymbol{Q} = \boldsymbol{F}. \tag{4}$$

The direct receptance α_{jj} at any coordinate j is defined as the generalized displacement at that coordinate due to a generalized force of unit amplitude and frequency ω applied at the same

coordinate. Application of Cramer's rule to equation (4) shows that

$$\alpha_{jj} = \frac{Q_j}{F_j} = \frac{\text{cofactor } S_{jj}}{|\boldsymbol{S}|} = \frac{\prod_{a=1}^{2n-2} (\mathrm{i}\omega - \lambda_a)}{\prod_{e=1}^{2n} (\mathrm{i}\omega - \lambda_e)}, \tag{5}$$

where the λ_e ($e = 1, 2, \ldots, 2n$) are the $2n$ complex ('resonance') eigenvalues of $\boldsymbol{S}(\mu, \mathrm{i}\omega)$ and the λ_a ($a = 1, 2, \ldots, 2n-2$) are the $2n-2$ complex ('anti-resonance') eigenvalues of $\boldsymbol{S}(\mu, \mathrm{i}\omega)$ with respect to the coordinate q_j. These anti-resonance eigenvalues are the (resonance) eigenvalues of the system that results from locking the jth coordinate q_j of the original system. It follows directly from equation (5) that the inverse direct receptance is

$$\frac{1}{\alpha_{jj}} = \frac{\prod_{e=1}^{2n} (\mathrm{i}\omega - \lambda_e)}{\prod_{a=1}^{2n-2} (\mathrm{i}\omega - \lambda_a)}. \tag{6}$$

Equation (5) also shows that as ω increases the locus of the direct receptance in the complex plane passes through the origin whenever $\mathrm{i}\omega$ is equal to a pure imaginary root λ_a of the system. Moreover it will assume an infinite value whenever $\mathrm{i}\omega$ equals a pure imaginary root λ_e. Equation (6), on the other hand, shows that the curve of inverse receptance possesses the opposite features. It assumes zero (or infinite) values whenever $\mathrm{i}\omega$ is equal to a pure imaginary root λ_e (or λ_a) of the system. It is assumed, of course, that none of the imaginary roots λ_e is exactly equal to an imaginary root λ_a.

Since the receptance curve assumes infinite values at the pure imaginary roots λ_e, it is of less interest here than that of the inverse receptance. This is because such roots as these occur at the boundary of flutter instability. Turning, then, to the inverse receptance curve $1/\alpha_{jj}(\mathrm{i}\omega)$ we note that the phase angle (strictly the argument) changes as ω increases continuously. This variation may be examined by applying the encirclement theory to equation (6), as with the transfer function of a control system.

When the imaginary variable $\mathrm{i}\omega$ traverses the usual Nyquist path (an infinite semi-circle covering the complete right hand side of the complex plane), the total change in the phase angle of the inverse receptance is found to be

$$|\Delta\phi \text{ of } 1/\alpha_{jj}(\mathrm{i}\omega)|_{\omega=-\infty}^{\omega=+\infty} = 2\pi(N_a - N_e - 1) \tag{7}$$

where N_a and N_e are the numbers of roots λ_a and λ_e with positive real parts respectively. Thus the inverse receptance curve encircles the origin $(N_a - N_e - 1)$ times as ω changes from $-\infty$ to $+\infty$. These encirclements will be in an anticlockwise direction as ϕ of the inverse receptance is usually measured from the positive real axis in a counterclockwise direction.

Application of the encirclement theory to oscillatory mechanical systems is not as convenient as it is for control systems, however. In the latter the number of encirclements is considered around the critical point $(-1, \mathrm{i}0)$ rather than the origin. Moreover poles (which correspond to the anti-resonance eigenvalues) with positive real parts seldom occur in transfer functions. These two features greatly simplify the application of encirclement theory. For its application to mechanical systems a modified approach is preferable.

All the complex resonance and anti-resonance eigenvalues occur in conjugate pairs since the matrices $\boldsymbol{A}$, $\boldsymbol{B}$ and $\boldsymbol{C}$, in equation (1), are real. Suppose there are no real resonance or

anti-resonance eigenvalues. Such a case would be more relevant for flutter instability. Equation (6) can then be rewritten as

$$1/\alpha_{jj}(\mu, \mathrm{i}\omega) = \frac{\prod_{e=1}^{n} (\mathrm{i}\omega - \lambda_e)\,(\mathrm{i}\omega - \bar{\lambda}_e)}{\prod_{a=1}^{n-1} (\mathrm{i}\omega - \lambda_a)\,(\mathrm{i}\omega - \bar{\lambda}_a)}, \tag{8}$$

where $\bar{\lambda}_e$ and $\bar{\lambda}_a$ are the complex conjugates of λ_e and λ_a respectively.

Figure 1 shows that the phase contribution of a conjugate pair of roots λ_e at μ_1 with negative real part increases continuously from 2π (at $\omega = 0$) to 3π (at $\omega = \infty$). On the other hand the contribution of another pair with positive real part at μ_2 decreases continuously from 2π (at $\omega = 0$) to π (at $\omega = \infty$).

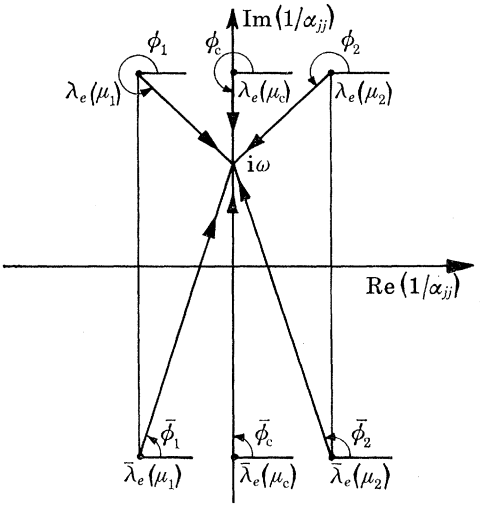

FIGURE 1. Phase contribution to inverse receptance of conjugate pairs of resonance eigenvalues, for driving frequency ω.

In other words the transition of one conjugate pair of roots λ_e from the left hand side to the right hand side of the imaginary axis produces a net decrease of 2π in the phase of $1/\alpha_{jj}$. (This result agrees with that of the encirclement theory in equation (7).) We therefore conclude that the contribution of a conjugate pair of roots λ_e is either a continuous increase or a continuous decrease of π in the phase of $1/\alpha_{jj}$ depending on whether the real part of the pair is negative or positive respectively. At the transition point where the pair is pure imaginary, at λ_c, the contribution is a *sudden* change from $-\pi$ to $+\pi$. This is again in agreement with equation (6) which shows that the curve of $1/\alpha_{jj}$ passes through the origin of the complex plane whenever $\mathrm{i}\omega$ equals one of the imaginary roots λ_e.

When investigating the stability of mechanical systems one is usually interested in the first instability boundary. The system, represented by equation (1) with its right hand side equal to zero, will usually be stable at low values of the parameter μ and consequently all the roots λ_e appear on the left hand side of the imaginary axis in the complex plane. The first critical value of μ is that at which the imaginary axis is first crossed by any of the eigenvalues. Under these circumstances a simple rule may be stated as follows:

'As the system departs from a stable state to an unstable state, its inverse-receptance curve shifts across the origin from the side of increasing phase difference to the side of decreasing

phase difference. At the flutter instability boundary the curve passes through the origin at the critical frequency.'

This rule is illustrated diagrammatically in figure 2. The validity of the rule rests upon the assumption made earlier that all the roots λ_e and λ_a have distinct imaginary parts. It will also be appreciated that the roots λ_a make contributions to the phase difference in the opposite direction from that of the roots λ_e, as may be seen from equations (7) and (8). Thus it is necessary to make allowance for the anti-resonance eigenvalues of the system when applying this rule.

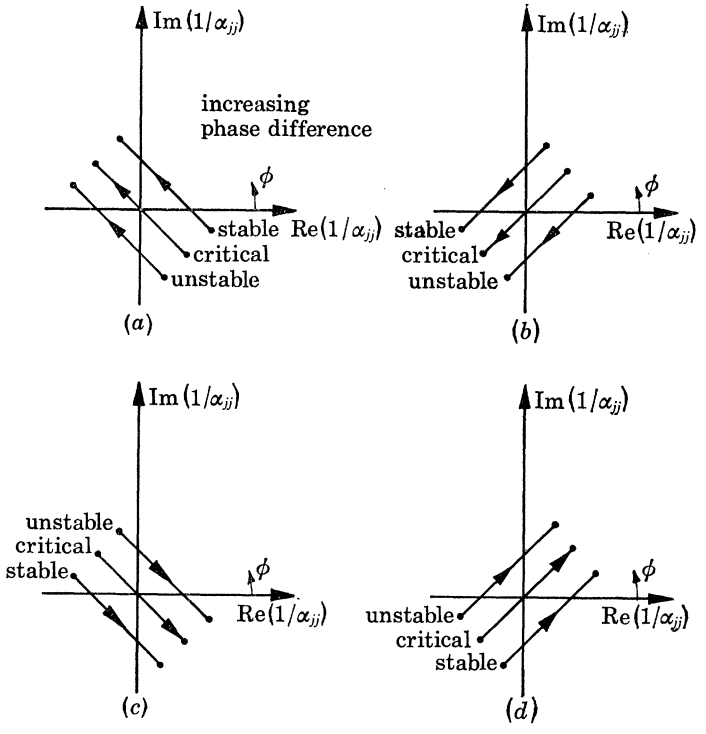

FIGURE 2. Shifting of the inverse receptance locus across the origin at the flutter instability boundary. The arrows indicate the directions of increasing ω.

Attention will now be focused on the particular system under investigation, namely the flexible tube conveying fluid. One of the main objectives will be to study the implications and application of the foregoing rule, as an instability criterion.

2. MATHEMATICAL FORMULATION

2.1. *The system and its distortion coordinates*

The system under investigation is shown diagrammatically in figure 3. It consists of a vertical flexible tube clamped at its upper end and free at its lower. Incompressible fluid flows downwards inside the tube at a constant velocity U. A light nozzle is fitted at the lower end of the tube. The velocity of fluid issuing through this nozzle in parallel flow is αU. An external harmonic force may be applied laterally to the tube.

In this paper, equations of motion are obtained by the use of Lagrange's equations in the form

$$\frac{\mathrm{d}}{\mathrm{d}t}\left(\frac{\partial T}{\partial \dot{q}_i}\right) - \frac{\partial T}{\partial q_i} + \frac{\partial V}{\partial q_i} = Q_i \quad (i = 1, 2, \ldots, n), \tag{9}$$

taking the system as the empty tube. That is to say, T and V will relate to the dry tube and both the fluid actions and the external exciting force will be accounted for in the quantities Q_i. In this, we shall adopt the approach that is commonly employed in aircraft flutter analysis.

It is necessary, of course, to choose a set of convenient generalized coordinates q_i which define the configuration at any instant. For the empty tube the lateral displacement $v(x, t)$ may be considered as the sum of displacements in the n lowest principal modes of a uniform elastic beam. We thus assume that

$$v(x, t) = \sum_{s=1}^{n} q_s(t)\, \phi_s(x) \tag{10}$$

where $\phi_s(x)$ is the sth characteristic function of the uniform cantilever, $q_s(t)$ is the associated generalized coordinate and n is the number of characteristic functions taken to represent the tube deflexion. Greater accuracy of representation in equation (10) is achieved by taking larger values of n.

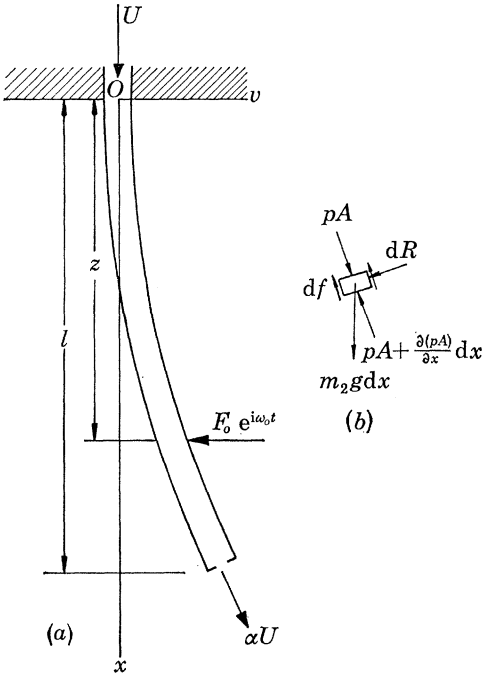

FIGURE 3. The system.

The theory that will be developed is a linear one in which lateral displacements v are considered first order small compared with x or l. It follows that the vertical displacement of the tube,

$$w = \frac{1}{2}\int_0^x \left(\frac{\partial v}{\partial x}\right)^2 \mathrm{d}x \quad (0 \leqslant x \leqslant l), \tag{11}$$

is second order small. The linear analysis implies that quantities of order greater than two in v are ignored in energy and work expressions.

2.2. *Energy and work expressions*

The kinetic energy of the empty tube is

$$T = \tfrac{1}{2} m_1 \int_0^l \left(\frac{\partial v}{\partial t}\right)^2 \mathrm{d}x, \tag{12}$$

where m_1 is the mass of the tube per unit length. (The nozzle fitted at the free end of the tube is assumed to possess negligible mass, its function being only that of increasing the fluid velocity from U to αU at the tube exit.) The potential energy is

$$V = \tfrac{1}{2}EI\int_0^l \left(\frac{\partial^2 v}{\partial x^2}\right)^2 \mathrm{d}x + \tfrac{1}{2}m_1 g\int_0^l\int_0^x \left(\frac{\partial v}{\partial x}\right)^2 \mathrm{d}x\,\mathrm{d}x, \tag{13}$$

where EI is the flexural rigidity. On substituting equation (10) into these energy expressions, so as to form the left hand side of equation (9), it is found that the equations of motion become

$$\sum_{s=1}^{n}\int_0^l \left[m_1\ddot{q}_s\phi_s\phi_i + EIq_s\phi_s''\phi_i'' + m_1 g q_s\int_0^x \phi_s'\phi_i' \mathrm{d}x\right]\mathrm{d}x = Q_i \quad (i = 1, 2, \ldots, n) \tag{14}$$

where an 'overdot' signifies differentiation with respect to time t and a prime means differentiation with respect to distance x.

The contribution made by the fluid flow to the generalized force Q_i is found from the work done by the fluid actions during a virtual displacement of the tube. These actions are of two sorts:

(i) a distributed force, comprising a reaction normal to the tube wall and also friction effects along it;

(ii) an axial tensile force applied to the inside surface of the nozzle plate.

We shall first find the magnitudes of these effects.

Figure 3 (b) shows an element of fluid which is instantaneously located at a distance x below the upper clamped end of the tube. The friction force along the tube bore is $\mathrm{d}f$ and the normal reaction of the tube wall is $\mathrm{d}R$. The gauge pressure in the fluid is p.

The transverse force applied by the fluid element to the inside of the tube in the direction $0v$ is

$$\mathrm{d}F_v = \mathrm{d}R + \mathrm{d}f\,\partial v/\partial x. \tag{15}$$

The absolute velocity of the fluid element in the lateral direction is

$$\left(\frac{\partial}{\partial t} + U\frac{\partial}{\partial x}\right)v$$

so that the equation of motion of that element in the lateral direction $0v$ is

$$\mathrm{d}R + \mathrm{d}f\frac{\partial v}{\partial x} + \frac{\partial}{\partial x}\left(pA\frac{\partial v}{\partial x}\right)\mathrm{d}x = -m_2\left(\frac{\partial}{\partial t} + U\frac{\partial}{\partial x}\right)^2 v\,\mathrm{d}x; \tag{16}$$

that is to say

$$\mathrm{d}F_v = -m_2\left(\frac{\partial}{\partial x} + U\frac{\partial}{\partial x}\right)^2 v\,\mathrm{d}x - \frac{\partial}{\partial x}\left(pA\frac{\partial v}{\partial x}\right)\mathrm{d}x. \tag{17}$$

The downward vertical force applied to the tube by this fluid element is

$$\mathrm{d}F_x = \mathrm{d}f - \mathrm{d}R\frac{\partial v}{\partial x}. \tag{18}$$

But vertical equilibrium of the fluid element requires that

$$m_2 g\,\mathrm{d}x - \mathrm{d}f + \mathrm{d}R\frac{\partial v}{\partial x} - \frac{\partial(pA)}{\partial x}\mathrm{d}x = 0. \tag{19}$$

Therefore

$$\mathrm{d}F_x = m_2 g\,\mathrm{d}x - \frac{\partial(pA)}{\partial x}\mathrm{d}x. \tag{20}$$

Having found expressions for the distributed forces $\mathrm{d}F_v$ and $\mathrm{d}F_x$ we may notice that neither contains a contribution from fluid friction. It was explained by Benjamin (1961) that motion of a tube of this sort is largely uninfluenced by friction between the fluid and the tube wall.

To find the last of the fluid actions (the force exerted on the upstream side of the nozzle and consequently on the tube cross section just above the nozzle plate) we consider the passage of fluid through the nozzle. We shall assume that the length of tube in which contraction of the flow takes place is small. The mass rate of flow through the nozzle is $m_2 U$, where $m_2 = \rho A$, i.e. the product of the fluid density and the internal cross-sectional area of the tube.

The gauge pressure above the nozzle is assumed to have an average value of p_l. The gauge pressure exerted by the fluid on the upper surface of the nozzle plate is assumed to have an average value of p_n.

Consideration of momentum flux shows that

$$p_l A - p_n(A - A_n) = m_2 U(\alpha U - U), \tag{21}$$

where A_n is the nozzle area and $\alpha = A/A_n$. Equilibrium of the nozzle plate in the vertical direction also requires that

$$p_n(A - A_n) = T_l, \tag{22}$$

where T_l is the tension in the tube at the nozzle. It follows that

$$p_l A - T_l = m_2 U^2(\alpha - 1). \tag{23}$$

As Benjamin (1961) pointed out, it is reasonable to assume that the flow in the tube is inviscid and incompressible. But in general, the flow is unsteady so that Bernoulli's equation can strictly be applied only in its extended form (see, for example, Duncan, Thom & Young 1960). The source of the unsteadiness, however, is the small deflexion $v(x, t)$ and it can readily be shown that its influence is negligible in the sense that Bernoulli's equation can still be applied in its elementary form without reference to the small perturbations of the flow due to flexure of the tube. Across the nozzle plate, therefore, we have

$$p_l + \tfrac{1}{2}\rho U^2 = \tfrac{1}{2}\rho\alpha^2 U^2$$

and so

$$p_l A = \tfrac{1}{2} m_2 U^2(\alpha^2 - 1). \tag{24}$$

Between them, equations (23) and (24) show that

$$T_l = \tfrac{1}{2} m_2 U^2(\alpha - 1)^2. \tag{25}$$

Bernoulli's equation can also be applied between a section distant x below the upper end of the tube, where the gauge pressure is p, and the section just above the nozzle plate which is distant l below the upper end. This gives

$$p + \rho g(l - x) = p_l,$$

or

$$pA + m_2 g(l - x) = p_l A, \tag{26}$$

and equation (24) now shows that

$$pA = \tfrac{1}{2} m_2 U^2(\alpha^2 - 1) - m_2 g(l - x). \tag{27}$$

If this last result is now substituted into equation (20) it is found that $\mathrm{d}F_x$ vanishes while equation (17) shows that

$$\mathrm{d}F_v = -m_2\left(\frac{\partial}{\partial t} + U\frac{\partial}{\partial x}\right)^2 v\,\mathrm{d}x - \tfrac{1}{2} m_2 U^2(\alpha^2 - 1)\frac{\partial^2 v}{\partial x^2}\mathrm{d}x - m_2 g\frac{\partial v}{\partial x}\mathrm{d}x + m_2 g(l - x)\frac{\partial^2 v}{\partial x^2}\mathrm{d}x. \tag{28}$$

Now the total fluid action on the tube consists of the sum of the $\mathrm{d}F_v$ over the tube length and the tension T_l at the lower end. The distributed force $\mathrm{d}F_v$ is in the same direction as the lateral deflexion of the tube, while the tension T_l acts tangentially to the tube at its lower extremity and is in the downward direction. The virtual work done by these fluid actions is therefore

$$\delta W = \int_0^l \delta v \frac{\partial F_v}{\partial x}\,\mathrm{d}x - \delta w_l T_l + \delta v_l T_l \left(\frac{\partial v}{\partial x}\right)_l, \tag{29}$$

where δw_l is the virtual displacement *upwards* at the lower end and $(\partial v/\partial x)_l$ is the slope of the tangent to the tube at its lower end.

The contribution to the ith generalized force is therefore

$$(Q_i)_{\text{fluid}} = \frac{\partial W}{\partial q_i} = \int_0^l \phi_i \frac{\partial F_v}{\partial x}\,\mathrm{d}x - \sum_{s=1}^{n} T_l \int_0^l q_s \phi_s' \phi_i'\,\mathrm{d}x + \sum_{s=1}^{n} T_l [q_s \phi_s'(l)\, \phi_i(l)]; \tag{30}$$

that is to say,

$$\begin{aligned}(Q_i)_{\text{fluid}} = \sum_{s=1}^{n} \int_0^l \{ & -m_2 \ddot{q}_s \phi_s \phi_i - 2m_2 U \dot{q}_s \phi_s' \phi_i - m_2 U^2 q_s \phi_s'' \phi_i - \tfrac{1}{2} m_2 U^2 (\alpha^2 - 1)\, q_s \phi_s'' \phi_i \\ & - m_2 g q_s \phi_s' \phi_i + m_2 g (l - x)\, q_s \phi_s'' \phi_i - \tfrac{1}{2} m_2 U^2 (\alpha - 1)^2\, q_s \phi_s' \phi_1' \}\,\mathrm{d}x \\ & + \sum_{s=1}^{n} \tfrac{1}{2} m_2 U^2 (\alpha - 1)^2 [q_s \phi_s'(l)\, \phi_i(l)] \quad (i = 1, 2, \ldots, n)\end{aligned} \tag{31}$$

and, since

$$\int_0^l \phi_s' \phi_i'\,\mathrm{d}x = \phi_s'(l)\, \phi_i(l) - \int_0^l \phi_i \phi_s''\,\mathrm{d}x, \tag{32}$$

it follows that

$$\begin{aligned}(Q_i)_{\text{fluid}} = \sum_{s=1}^{n} \int_0^l \{ & -m_2 \ddot{q}_s \phi_s - 2m_2 U \dot{q}_s \phi_s' - m_2 \alpha U^2 q_s \phi_s'' \\ & - m_2 g q_s \phi_s' + m_2 g (l - x)\, q_s \phi_s'' \} \phi_i\,\mathrm{d}x \quad (i = 1, 2, \ldots, n).\end{aligned} \tag{33}$$

To obtain the contribution, $(Q_i)_{\text{exc}}$, to the generalized force component Q_i that is attributable to the excitation, we first assume that the tube is acted upon by a general force of intensity $f(x)$ per unit length. For a virtual displacement δv of the tube, the work done is

$$\delta W = \int_0^l \delta v f(x)\,\mathrm{d}x. \tag{34}$$

On substituting for v in equation (34) from equation (10) it is found that the generalized force component is

$$(Q_i)_{\text{exc}} = \frac{\partial W}{\partial q_i} = \int_0^l \phi_i f(x)\,\mathrm{d}x \quad (i = 1, 2, \ldots, n). \tag{35}$$

2.3. *The equations of motion*

To form the equations of motion (14), we first note that

$$\int_0^l \phi_s'' \phi_i''\,\mathrm{d}x = \int_0^l \phi_s^{\mathrm{iv}} \phi_i\,\mathrm{d}x. \tag{36}$$

Write

$$\int_0^x \phi_s'' \phi_i\,\mathrm{d}x = J(x)$$

PHILOSOPHICAL TRANSACTIONS OF THE ROYAL SOCIETY A MATHEMATICAL, PHYSICAL & ENGINEERING SCIENCES

and note that $\phi_s'(0)\,\phi_i(0) = 0$. Then, integrating by parts twice successively, we obtain

$$\begin{aligned}\int_0^l\int_0^x \phi_s'\phi_i'\,\mathrm{d}x\,\mathrm{d}x &= \int_0^l [|\phi_s'\phi_i|_0^x - J(x)]\,\mathrm{d}x\\ &= \int_0^l \phi_s'\phi_i\,\mathrm{d}x - |xJ(x)|_0^l + \int_0^l \phi_s''\phi_i x\,\mathrm{d}x\\ &= \int_0^l [\phi_s'\phi_i - (l-x)\,\phi_s''\phi_i]\,\mathrm{d}x. \end{aligned} \tag{37}$$

If, now, the expressions (33) and (35) are introduced on the right hand side of equation (14) and the results (36) and (37) are introduced on the left, it is found that

$$\begin{aligned}\sum_{s=1}^{n}\int_0^l [(m_1+m_2)\,\ddot{q}_s\phi_s + 2m_2U\dot{q}_s\phi_s' + \alpha m_2U^2q_s\phi_s'' + EIq_s\phi_s^{\mathrm{iv}} + (m_1+m_2)\,gq_s\phi_s'\\ - (m_1+m_2)\,g(l-x)\,q_s\phi_s'']\,\phi_i\,\mathrm{d}x = \int_0^l f(x)\,\phi_i\,\mathrm{d}x \quad (i=1,2,\ldots,n).\end{aligned} \tag{38}$$

This is a set of n equations that describe the motion of the system under consideration.

It may be derived by other methods (Wahed 1969) – e.g. by direct application of Newton's laws in conjunction with Galerkin's method or by the employment of an adaptation of Lagrange's equations (Benjamin 1961).

2.4. *Dimensionless parameters and matrix formulation*

It is convenient to put the equation of motion into a dimensionless form. Suitable dimensionless parameters are

$$\left.\begin{aligned} X = \frac{x}{l};\quad V = \frac{v}{l};\quad T = \left[\frac{EI}{(m_1+m_2)\,l^4}\right]^{\frac{1}{2}}t;\quad \zeta = \frac{fl^3}{EI};\\ \mu = Ul\left(\frac{m_2}{EI}\right)^{\frac{1}{2}};\quad \beta = 2\left(\frac{m_2}{m_1+m_2}\right)^{\frac{1}{2}};\quad \gamma = \frac{(m_1+m_2)\,gl^3}{EI}.\end{aligned}\right\} \tag{39}$$

When these parameters are used in equation (38) it is found after rearrangement of the terms that

$$\begin{aligned}\sum_{s=1}^{n}\left[\ddot{P}_s\int_0^1 \Phi_i\Phi_s\,\mathrm{d}X + \mu\beta\dot{P}_s\int_0^1 \Phi_i\Phi_s'\,\mathrm{d}X + P_s\int_0^1 [\Phi_i\Phi_s^{\mathrm{iv}} + \mu^2\alpha\Phi_i\Phi_s'' + \gamma\{(X-1)\,\Phi_i\Phi_s'' + \Phi_i\Phi_s'\}]\,\mathrm{d}X\right]\\ = \int_0^1 \zeta\Phi_i\,\mathrm{d}X, \quad (i=1,2,\ldots,n)\end{aligned} \tag{40}$$

where now P_s is a dimensionless generalized co-ordinate (a function of dimensionless time T) that replaces q_s, and Φ_i is the ith dimensionless characteristic function of a uniform beam (being a function of the dimensionless quantity X). The 'overdot' refers now to differentiation with respect to T and the prime indicates differentiation with respect to X.

The significance of each of the parameters in equation (39) is as follows:

α is the nozzle parameter (where $\alpha \geqslant 1$)

β is the mass parameter, a measure of the total mass per unit length accounted for by the fluid (and $0 \leqslant \beta < 2$)

γ is the weight parameter, a measure of the stiffness attributable to gravity (where $\gamma \geqslant 0$)

μ is the velocity parameter, a measure of fluid velocity inside the tube (and $\mu \geqslant 0$)

ζ is the excitation parameter, a measure of the external harmonic force applied on the tube ($\zeta \geqslant 0$).

The integrals in equation (40) may readily be evaluated on reference to Bishop & Johnson (1960). When their values are substituted into the equations and the terms are rearranged it is found that

$$\boldsymbol{I}\ddot{\boldsymbol{P}} + \mu\beta\boldsymbol{E}\dot{\boldsymbol{P}} + [\boldsymbol{A} + \mu^2\alpha\boldsymbol{G} + \gamma\boldsymbol{H}]\,\boldsymbol{P} = \boldsymbol{R} \tag{41}$$

where $\boldsymbol{I}$ is the unit matrix of order n, $\boldsymbol{P}$ is the column matrix $\{P_1, P_2, \ldots, P_n\}$ and $\boldsymbol{E}$, $\boldsymbol{A}$, $\boldsymbol{G}$ and $\boldsymbol{H}$ are square matrices of order n given by:

$$\left.\begin{aligned}
E_{rs} &= \int_0^1 \Phi_r \Phi_s' \,\mathrm{d}X = \frac{4}{\theta_{rs}^2 + (-1)^{r+s}};\\
E_{rr} &= \int_0^1 \Phi_r \Phi_r' \,\mathrm{d}X = 2;\\
A_{rs} &= 0; \quad A_{rr} = \int_0^1 \Phi_r \Phi_r^{\mathrm{iv}} \,\mathrm{d}X = \lambda_r^4;\\
G_{rs} &= \int_0^1 \Phi_r \Phi_s'' \,\mathrm{d}X = \frac{4(\sigma_r\lambda_r - \sigma_s\lambda_s)}{\theta_{rs}^2 - (-1)^{r+s}};\\
G_{rr} &= \int_0^1 \Phi_r \Phi_r'' \,\mathrm{d}X = \sigma_r\lambda_r(2 - \sigma_r\lambda_r);\\
H_{rs} &= \int_0^1 [(X-1)\,\Phi_r\Phi_s'' + \Phi_r\Phi_s']\,\mathrm{d}X\\
&= C_{rs}[\theta_{rs}^2(2 + C_{rs}) - \theta_{rs}^2(\sigma_r\lambda_r - \sigma_s\lambda_s) - (-1)^{r+s}(4 + C_{rs})];\\
H_{rr} &= \int_0^1 [(X-1)\,\Phi_r\Phi_r'' + \Phi_r\Phi_r']\,\mathrm{d}X\\
&= \tfrac{1}{2}\sigma_r^2\lambda_r^2 - \sigma_r\lambda_r + 2.
\end{aligned}\right\} \tag{42}$$

In equations (42) σ_r and λ_r are the constants appearing in the characteristic functions of beam vibration (see Bishop & Johnson 1960) and

$$\theta_{rs} = \frac{\lambda_r}{\lambda_s}; \quad C_{rs} = \frac{4}{\theta_{rs}^4 - 1}. \tag{43}$$

The column matrix $\boldsymbol{R}$ is obtained by integration of the right hand side of equation (40). Each integral represents the work done by the appropriate force function in the corresponding mode of deflexion. It can be evaluated only when the force distribution is known, of course.

In the special case where the tube is subjected to a concentrated harmonic force $F_0\,\mathrm{e}^{\mathrm{i}\omega_0 t}$ applied at a distance z below the clamped end (as in figure 3), the non-dimensional force may be found as follows:

$$\int_0^1 \zeta\Phi_i \,\mathrm{d}X = \int_0^1 \frac{fl^3}{EI}\Phi_i \,\mathrm{d}X$$

and since $f = 0$ everywhere except at $x = z$ and

$$\int_0^1 fl \,\mathrm{d}X = \int_0^l f \,\mathrm{d}x = F_0,$$

it follows that

$$R_i = \frac{F_0 l^2}{EI}\Phi_i(Z)\,\mathrm{e}^{\mathrm{i}\omega T}, \tag{44}$$

where the dimensionless frequency is

$$\omega = \frac{\omega_0 t}{T} = \omega_0\left[\frac{(m_1 + m_2)\,l^4}{EI}\right]^{\frac{1}{2}}. \tag{45}$$

The equation of motion is therefore

$$\boldsymbol{I}\ddot{\boldsymbol{P}}+\mu\beta\boldsymbol{E}\dot{\boldsymbol{P}}+(\boldsymbol{A}+\alpha\mu^2\boldsymbol{G}+\gamma\boldsymbol{H})\,\boldsymbol{P}=F\boldsymbol{\Phi}_z\,\mathrm{e}^{\mathrm{i}\omega T}, \tag{46}$$

where $F=F_0l^2/EI$ and $\boldsymbol{\Phi}_z\equiv\{\Phi_1(Z),\Phi_2(Z),\ldots,\Phi_n(Z)\}$.

2.5. *Representation of structural damping forces*

Apart from the hydrodynamic damping caused by water flowing inside the tube, and described by the term $\mu\beta\boldsymbol{E}\dot{\boldsymbol{P}}$ in the equation of motion (equation (41)), two other types of damping will be considered, namely viscous and Kelvin damping. Both of these types are commonly used in the study of free vibration problems and it is of interest to see how they affect the stability boundary of our system.

Viscous damping may be considered to account for the external damping on the tube surface and the damping at its clamped end. The Kelvin damping is widely accepted as representing internal damping in rubber material (see Payne & Scott 1960). Paidoussis (1970) considered both the external and internal dampings in such a system to be either viscous or hysteretic.

The viscous damping is accounted for in the usual way by employing a dissipation function in Lagrange's equations. Kelvin damping, on the other hand, is considered by simply replacing the Young modulus E by the expression $(E+\nu\,\partial/\partial t)$, where ν is the so-called coefficient of dynamic viscosity of the rubber. If the foregoing procedure is followed, the complete equations of motion are found to be

$$\sum_{s=1}^{n}\Big[\ddot{P}_s\int_0^1\Phi_i\Phi_s\,\mathrm{d}X+\dot{P}_s\int_0^1(\mu\beta\Phi_i\Phi_s'+\eta\Phi_i\Phi_s+\kappa\Phi_i\phi_s^{\mathrm{iv}})\,\mathrm{d}X$$
$$+P_s\int_0^1[\Phi_i\Phi_s^{\mathrm{iv}}+\mu^2\alpha\Phi_i\Phi_s''+\gamma\{(X-1)\,\Phi_i\Phi_s''+\Phi_i\Phi_s'\}]\,\mathrm{d}X\Big]=\int_0^1\zeta\Phi_i\,\mathrm{d}X,$$
$$(i=1,2,\ldots,n) \tag{47}$$

where η and κ are dimensionless parameters for the viscous and Kelvin damping such that

$$\eta=\frac{bl^2}{[EI(m_1+m_2)]^{\frac{1}{2}}};\quad \kappa=\frac{\nu}{l^2}\left[\frac{I}{(m_1+m_2)\,E}\right]^{\frac{1}{2}}, \tag{48}$$

b being a constant specifying the viscous damping force per unit velocity per unit length.

An interesting comparison may be drawn between the viscous and Kelvin dampings. The viscous and Kelvin damping terms in equation (47) are

$$\eta\dot{P}_s\int_0^1\Phi_i\Phi_s\,\mathrm{d}X,\quad \lambda_s^4\kappa\dot{P}_s\int_0^1\Phi_i\Phi_s\,\mathrm{d}X$$

respectively (see Bishop & Johnson 1960). Evidently then, a viscous damping coefficient η is equivalent to a Kelvin damping coefficient κ multiplied by λ_s^4 in respect of the sth mode of cantilever vibration. It follows that whereas the viscous damping affects the different modes with the same intensity, Kelvin damping affects the higher modes more than the lower ones, its intensity being proportional to the square of the natural frequency of the mode (since the sth natural frequency ω_s is proportional to λ_s^2). This characteristic of Kelvin damping is very useful for the system under investigation as it was noticed in the course of experiments that high modes were damped much more heavily than low ones.

Equation (47) is of the same form as (40). To arrive at the equation of motion comparable with (46), we make use of this last result, obtaining

$$\boldsymbol{I}\ddot{\boldsymbol{P}} + (\mu\beta\boldsymbol{E} + \eta\boldsymbol{I} + \kappa\boldsymbol{S})\,\dot{\boldsymbol{P}} + (\boldsymbol{A} + \alpha\mu^2\boldsymbol{G} + \gamma\boldsymbol{H})\,\boldsymbol{P} = F\boldsymbol{\Phi}_Z\,\mathrm{e}^{\mathrm{i}\omega T}, \tag{49}$$

where

$$\boldsymbol{S} = \mathrm{diag}\,(\lambda_1^4, \lambda_2^4, \ldots, \lambda_n^4). \tag{50}$$

3. Numerical analysis

3.1. *Method of solution and calculation procedure*

For the free vibration analysis it is helpful to allow first for fluid damping only and then to show how the results are modified by the admission of other types. Accordingly, a solution of equation (46) is assumed in the form

$$\boldsymbol{P} = \boldsymbol{K}\,\mathrm{e}^{\sigma T}, \tag{51}$$

where $\boldsymbol{K}$ is an unknown vector $\{K_1, K_2, \ldots, K_n\}$ and σ is an unknown dimensionless complex frequency (not to be confused with the constant σ_r in the beam characteristic function which always appears multiplied by λ_r). The condition for a non-trivial solution to exist is therefore

$$|\sigma^2\boldsymbol{I} + \sigma(\mu\beta\boldsymbol{E}) + (\boldsymbol{A} + \mu^2\alpha\boldsymbol{G} + \gamma\boldsymbol{H})| = 0. \tag{52}$$

On expansion, the determinant yields a polynomial of degree $2n$ in σ and there are thus $2n$ roots. These roots may be real; alternatively they may be imaginary or complex, in which case they form conjugate pairs since the characteristic polynomial has only real coefficients. Dynamic instability prevails when either a real root or the real part of a complex root is positive. When a real root is positive the system loses stability by 'divergence'. When the real part of a complex root is positive stability is lost by oscillatory motion of increasing amplitude, termed 'flutter'. The nature of the vector $\boldsymbol{K}$ will largely be ignored here as we shall concern ourselves mainly with the instability boundary.

The calculation procedure was the straightforward one of finding all the roots of the characteristic equation. First the elements of the matrices $\boldsymbol{E}$, $\boldsymbol{A}$, $\boldsymbol{G}$ and $\boldsymbol{H}$ were calculated by direct substitution in equation (42) with the use of the characteristic functions of cantilever beams. For series of values α, β and γ, the roots were then computed and plotted on the complex plane to obtain appropriate root locus diagrams. Whenever a branch of the root locus diagram crossed the imaginary axis from left to right a flutter instability boundary was indicated. The value of μ at the crossing point was the critical (dimensionless) velocity μ_c and the ordinate of the crossing point on the imaginary axis indicated the critical (dimensionless) frequency σ_c, i.e. the frequency of sustained oscillation at the instability boundary.

A similar approach to this was employed when allowance is made for viscous and/or Kelvin damping. Then values have to be chosen in some way for the constants η and κ. It is necessary in this case to start from equation (49), taking a null matrix on the right hand side.

For the forced vibration analysis a particular integral of equation (46) was assumed in the form:

$$\left.\begin{aligned} P_1 &= h_1\,\mathrm{e}^{\mathrm{i}(\omega T + c_1)} \\ P_2 &= h_2\,\mathrm{e}^{\mathrm{i}(\omega T + c_2)} \\ &\cdots\cdots\cdots\cdots\cdots \\ P_n &= h_n\,\mathrm{e}^{\mathrm{i}(\omega T + c_n)} \end{aligned}\right\} \tag{53}$$

where $h_1, h_2, \ldots, h_n$ are amplitudes and $c_1, c_2, \ldots, c_n$ are phase angles defining a mode of vibration.

It is evidently necessary that

$$[(\boldsymbol{A}-\omega^2\boldsymbol{I}+\mu^2\alpha\boldsymbol{G}+\gamma\boldsymbol{H})+\mathrm{i}\omega\mu\beta\boldsymbol{E}]\,\boldsymbol{u}=F\boldsymbol{\Phi}_z, \tag{54}$$

in which $\boldsymbol{u}$ is a column matrix whose elements are

$$u_r = h_r\,\mathrm{e}^{\mathrm{i}c_r} \quad (r=1,2,\ldots,n). \tag{55}$$

For any particular value of fluid velocity μ and excitation frequency ω, equation (54) can be solved for $\boldsymbol{u}$. When the elements of $\boldsymbol{u}$ are known, equations (53) give the values $P_1, P_2, \ldots, P_n$ by direct substitution; that is to say they give the matrix $\boldsymbol{P}$. Having obtained $\boldsymbol{P}$ it is possible to obtain the forced displacement of the tube at any distance $Y = y/l$ from the clamped end. This is

$$V(Y) = \sum_{r=1}^{n} \Phi_r(Y)\,h_r\,\mathrm{e}^{\mathrm{i}(\omega T+c_r)}. \tag{56}$$

It is now possible to write down an expression for the general cross harmonic receptance between two sections y and z. This is the complex displacement caused by a harmonic force of unit amplitude and (in nondimensional terms) it is

$$\alpha_{YZ} = \frac{1}{F}\sum_{r=1}^{n} \Phi_r(Y)\,h_r\,\mathrm{e}^{\mathrm{i}c_r}. \tag{57}$$

When both the displacement and the force producing it are at the same point we have the dimensionless direct receptance given by

$$\alpha_{ZZ} = \frac{1}{F}\sum_{r=1}^{n} \Phi_r(Z)\,h_r\,\mathrm{e}^{\mathrm{i}c_r}. \tag{58}$$

The procedure for calculating these receptances is straightforward. The elements of the matrices $\boldsymbol{E}$, $\boldsymbol{A}$, $\boldsymbol{G}$ and $\boldsymbol{H}$ were first calculated by using equations (49). Their values were then substituted in equation (54) which then became a set of n simultaneous equations with complex coefficients in the unknowns $u_1, u_2, \ldots, u_n$, which could be solved on the digital computer.

The procedure was repeated for progressively increasing values of the excitation frequency ω for different values of fluid velocity μ. Values of the receptance were then plotted on the complex plane to show its variation with the excitation frequency at each value of the fluid velocity. The curves were drawn in accordance with the usual practice in plotting harmonic response diagrams. Thus the receptance at any point is represented by the vector connecting the origin to that point. The positive real axis represents the direction of the applied force and the phase angle by which the displacement lags behind the force is measured from the positive real axis in a clockwise direction.

By working from equation (49), rather than (46), allowance can be made in just the same way for internal and external damping of the tube. The introduction of values for the parameters η and κ considerably increases the problems of displaying the resulting response loci however. In the present investigation, therefore, only fluid damping (which is certainly of greatest importance) was examined in studies of forced vibration.

3.2. *Numerical values*

In the free vibration analysis the main object of the calculations was to clarify the roles played by the three parameters α, β and γ; for each of these quantities represents a load of a distinct dynamic type. The parameter α represents a non-conservative compressive follower force at the

end of the tube. The parameter β governs a velocity-dependent lateral load distributed over the whole tube length.† The parameter γ represents a distributed weight loading that is also distributed over the tube length. The effect on the instability is investigated when each of these parameters is varied separately. Allowance was then made for Kelvin and viscous damping separately.

In these investigations the tube was considered to have four bending degrees of freedom. In other words, n in equation (2) was taken equal to 4. Analysis with five degrees of freedom was also tried in a particular case. The lowest four branches of the root locus were affected so slightly that it was not thought to be worth while to proceed. While this may perhaps be thought to cast some doubts on the accuracy of some predictions concerning the higher order modes, it will be appreciated that each added degree of freedom greatly increased the complexity of the calculations whereas simplicity was a main objective.

The results to be presented in the analysis of forced vibration were computed for a particular system in which $\alpha = 3.0$; $\beta = 0.9$ and $\gamma = 5$. There is nothing special about these particular values of the parameters. The only reason for their choice is that they produced a convenient system for numerical calculations. Two instability boundaries were found within a reasonable range of fluid velocity.

4. Theory of free vibration

4.1. *Effect of the weight parameter* γ

The root locus diagrams for $\gamma = 0$, 20 and 160 at $\alpha = 1.0$ and $\beta = 1.244$ are shown in figures 4 (a)–(c) respectively. Only the upper half of the complex plane is shown. The lower half is a mirror image of the upper one since the complex roots occur in conjugate pairs.

At $\gamma = 0$, where the weight effect is nil (so that either the tube is horizontal or it has a very high flexural rigidity), figure 4 (a) shows that the tube loses stability by flutter as the second branch of the locus crosses the imaginary axis. By the 'second branch' is meant the continuation of that branch which starts at the second lowest frequency on the imaginary axis when $\mu = 0$. This continuation does not have the second lowest characteristic frequency at the instability boundary. For this reason we shall refer to it as the second branch and not the 'second mode' as other authors have called it.

At $\gamma = 20$, figure 4 (b) shows that the second branch remains in the stable region at least up to $\mu = 12$. But it is the third branch which now crosses the imaginary axis to the unstable side. As γ is increased further, the third branch turns back nearer to the imaginary axis until it actually crosses it back to the stable side. This indicates a limited unstable region after which the tube regains its stability in all its four branches. A second instability boundary then appears in the fourth branch at a higher frequency (see figure 4 (c) and 5 (a)). At $\gamma = 160$ the third branch loop is completely in the stable side and the tube loses stability in the fourth branch. The weight parameter γ therefore changes the unstable branch successively from the second to the third to the fourth.

As we have seen, it appears to be a matter of some importance to retain the identities of the branches of the root locus, and not merely to refer to 'modes' in order of ascending frequency. When the stability of a continuous system is being examined, the higher the order of a branch

† Strictly the term representing this load in the equation of motion appears multiplied by $\mu\beta$ but adjustment of β allows the change of this load irrespective of the value of μ.

PHILOSOPHICAL TRANSACTIONS OF THE ROYAL SOCIETY A MATHEMATICAL, PHYSICAL & ENGINEERING SCIENCES

investigated the more assumed modal shapes are needed for the same degree of accuracy. In fact, since the higher values of γ used in figure 4 involve the instability associated with higher order branches, a larger number of modes in the analysis is necessary if accuracy of the results is to be maintained. This is a point of some importance since certain instability studies of continuous systems have been made with a two-mode analysis, i.e. by assuming the system to possess two degrees of freedom only.

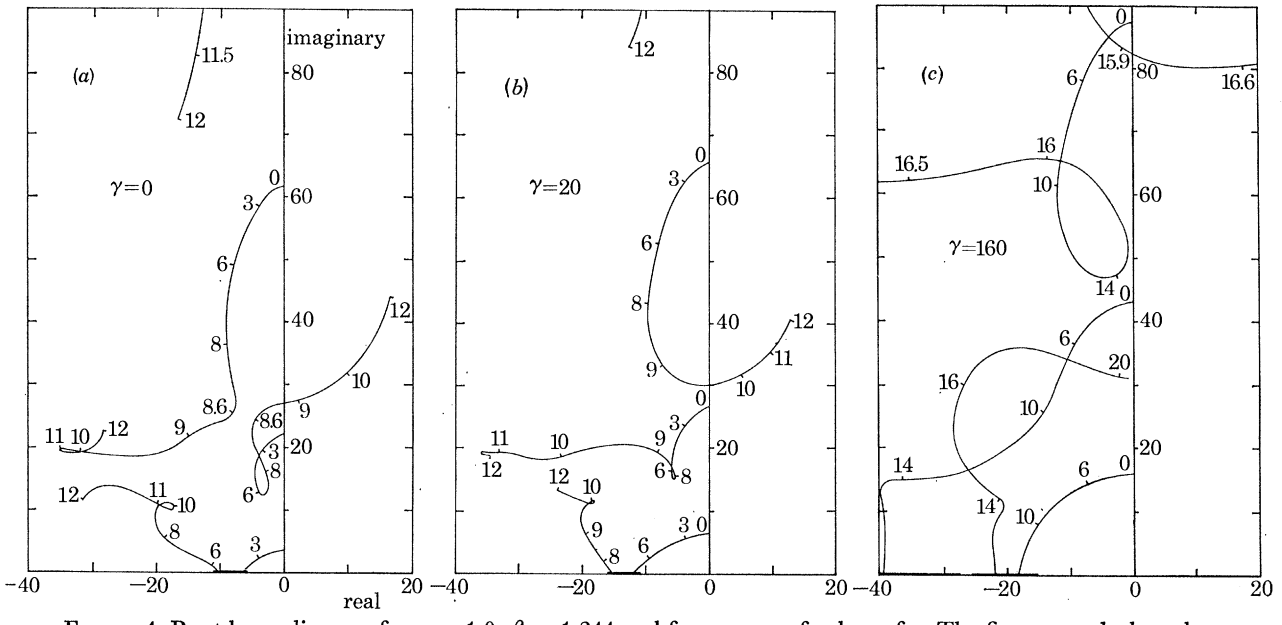

FIGURE 4. Root locus diagram for $\alpha = 1.0$, $\beta = 1.244$ and for a range of values of γ. The figures marked on the branches are values of μ.

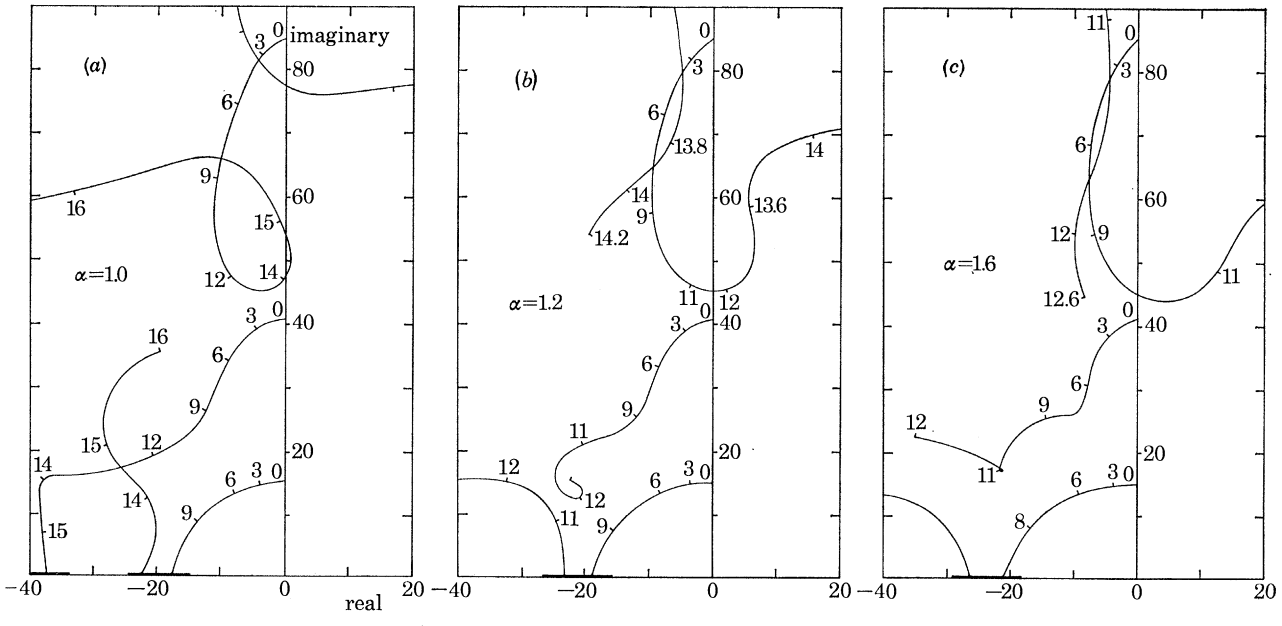

FIGURE 5. Root locus diagram for $\beta = 1.244$, $\gamma = 140$ and for a range of values of α. The figures marked on the branches are values of μ.

It may be that the trend we have seen in figure 4 continues to higher branches as γ is increased further. That is to say, perhaps each branch in turn behaves like the third–first crossing the imaginary axis to the 'unstable side', there forming a loop and finally shifting back to the 'stable side'. But, as we have mentioned, this point can only be examined logically with a successively increased number of assumed degrees of freedom.

On comparing figure 4 (a)–(c) we notice that in general γ raises the characteristic frequencies of the system in all the branches at any particular value of μ. This is seen clearly when the characteristic frequencies on the different branches at $\mu = 0$, 6 and 10 are contrasted between figure 4 (b) where $\gamma = 20$, and figure 4 (c) where $\gamma = 160$. Thus at $\gamma = 20$, the lowest three natural frequencies are about 7, 27 and 66 when $\mu = 0$, whereas when $\gamma = 160$ the frequencies at $\mu = 0$ are approximately 16, 43 and 88 respectively. Similar conclusions may be reached for finite values of μ, so we find that γ is essentially a stiffness parameter.

The locus branches that meet the real axis of the plane need some clarification. As mentioned before there is a mirror image about the real axis for each complex branch. When a branch from the upper half of the plane meets the real axis its conjugate therefore meets the axis at the same point. There are then two purely real roots on the axis. These real roots remain on the axis for some range of velocity, the appropriate points first moving away from each other and then moving closer together again until they coalesce before departing from the real axis to form two conjugate roots as before. The movement of the two roots on the real axis is indicated by a solid line on the axis as seen in figures 4 (a)–(c).

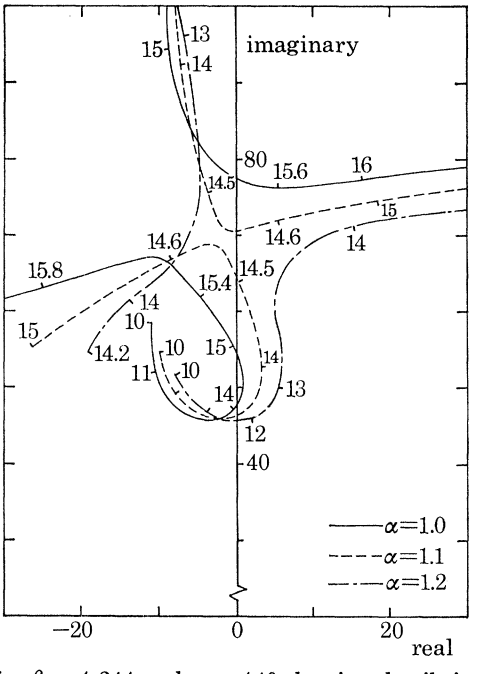

FIGURE 6. Root locus diagrams for $\beta = 1.244$ and $\gamma = 140$ showing details in the region of instability transfer between the third and fourth branches. The figures marked on the branches are values of μ.

4.2. *Effect of the nozzle parameter* α

Figures 5 (a)–(c) are the root locus diagrams for values of $\alpha = 1.0$, 1.2 and 1.6, with $\beta = 1.244$ and $\gamma = 140$. These figures show that, generally speaking, increasing α has the effect of shifting the stable roots on the branches nearer to the imaginary axis and thus decreasing the effective

(hydrodynamic) damping in the system at any fluid velocity. At $\mu = 0$, the branches start on the imaginary axis at the same values as before since α loses its significance when there is no fluid flow.

Figures 5 (a) and (b) show that adjustment of α can cause transference of the instability from one branch in the root locus to another. Thus figure 5 (a) shows that as the flow rate is increased a limited instability occurs in the third branch (which may disappear altogether at a different value of β as will be seen later); this is followed by stability again and then by instability in the fourth branch. Figure 5 (b) on the other hand shows that instability occurs in the third branch and that the fourth is always stable. We shall refer to this phenomenon as 'instability transference' between the third and fourth branches. It is necessary to recall, however, that, strictly, more degrees of freedom are required to ensure the accuracy of the predictions of these high order branches, although it is unlikely that the admission of more terms will alter results qualitatively.

The instability transference of figures 5 (a) and (b) is illustrated in more detail in figure 6 where only the two relevant branches are shown. The roots loci for $\alpha = 1.0$ and $\alpha = 1.2$ are contrasted with that for the intermediate value $\alpha = 1.1$. It is seen that the curves display a form of degeneracy akin to that associated with nodal lines in receptance diagrams.

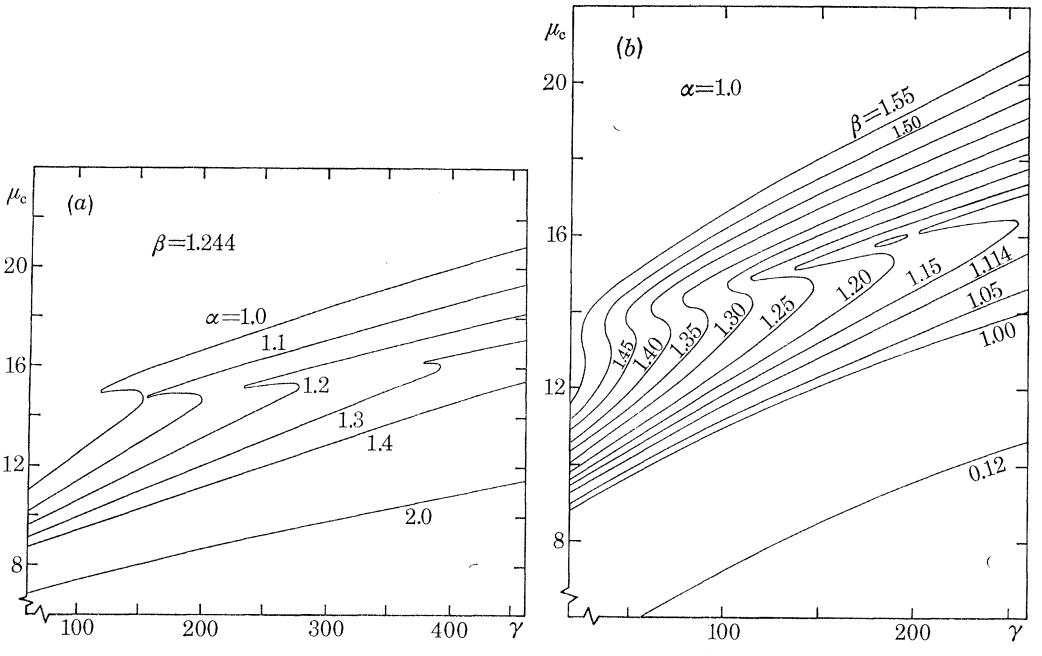

FIGURE 7. Variation of nondimensional critical velocity μ_c.

4.3. *Stability charts*

It is of interest to examine the effects of α, β and γ at the instability boundary, on the values of the critical velocity μ_c and the critical frequency σ_c. Figures 7 (a) and (b) show stability charts for various combinations of the parameters. From figure 7 (a) it is seen that the destabilizing effect of α is greater than the stabilizing effect of γ in the sense that a percentage increase in α results in a decrease in μ_c which is numerically greater than the increase caused by an equal percentage increase in γ. We also see that the destabilizing effect of α is greater when γ is large than when it is small. The inflexion in the instability boundary is shifted to higher values of γ by

increasing α. It is also diminished during its shift until it eventually disappears at sufficiently high values of α and γ. The importance of the inflexion is that its presence indicates that α has a *limited* stabilizing effect.

Figure 7 (b) shows the interaction between the mass ratio parameter β and the weight parameter γ. Values of β indicated in the figures are in the middle of the possible range ($0 \leqslant \beta \leqslant 2.0$) where the interaction is most pronounced. It is seen that β has a strong stabilizing effect which increases at high values of γ. For the same change in γ the percentage increase in μ_c is higher at higher values of β.

The inflexion in the instability boundary is sensitive to the value of β. While there is a very steep rise over a small range of γ when $\beta = 1.55$, the region occupies a wide range of γ at $\beta = 1.15$.

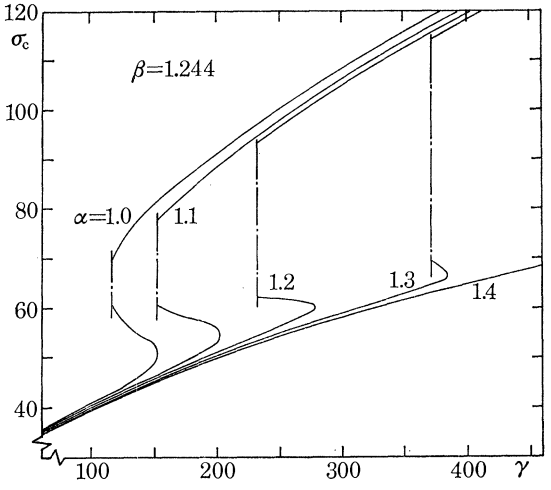

FIGURE 8. Variation of the critical frequency σ_c.

Special interest centres on small values of β where the inflexion region is sufficiently remote to allow a uniform rate of increase of μ_c with γ. Consider the limiting case where m_1 is so large that $\beta \approx 0$ while μ has a finite value. The (hydrodynamic) damping term in equation (41) will then disappear and the roots of the resulting characteristic equation (52) will all be real or imaginary (but not complex). This means that the root locus branches sweep along the imaginary axis as μ increases until a pair coalesce at some frequency. Instability takes place thereafter when these coalescing roots depart from the imaginary axis in two branches, one to the left (stable) and one to the right (unstable). This is the usual mechanism of instability in undamped systems and it is referred to as 'instability by coalescence of frequencies'. Coalescence of roots may not occur on the imaginary axis; in such a case the roots sweep down the imaginary axis until they reach the origin and then move sideways on the real axis on both sides. This is identified with divergence rather than a flutter.

Variation of the critical frequency σ_c has a different pattern as shown in figure 8. With $\alpha = 1$ variation of σ_c with γ is almost continuous with an inflexion region similar to that in the critical velocity curves. As γ increases the inflexion region moves to higher ranges of γ and suffers a sudden jump from low frequency to the high one. The critical frequency curves lose their continuity and appear to be chopped off. The reason for this is that the fourth branch crosses the imaginary axis to the unstable side at a frequency higher than that at which the third branch regains its stability as shown in figure 5 (a). Apart from this 'chopping off' effect, the influence

of α on the critical frequency is smaller than its effect on the critical velocity. Variation of β was found to produce similar effects on the relationship between σ_c and γ.

4.4. *The effects of internal and external damping*

Figure 9 shows the computed variation of μ_c with γ, for $\kappa = 0$, 0.001, 0.002 and 0.003. The effect of Kelvin damping is seen to be small at low values of γ where μ_c is hardly affected by the presence of damping. As γ increases the Kelvin damping destabilizes the system significantly, the effect being most pronounced in the inflexion region where μ_c now depends monotonically on γ. The destabilizing effect of Kelvin damping is not maintained at all values of γ and we see that the instability boundary curves of the damped system eventually intersect with the curve for the undamped system. The value of γ at which intersection takes place increases with increasing values of κ. After the intersection point it appears that Kelvin damping now has a stabilizing effect which increases with increasing values of γ.

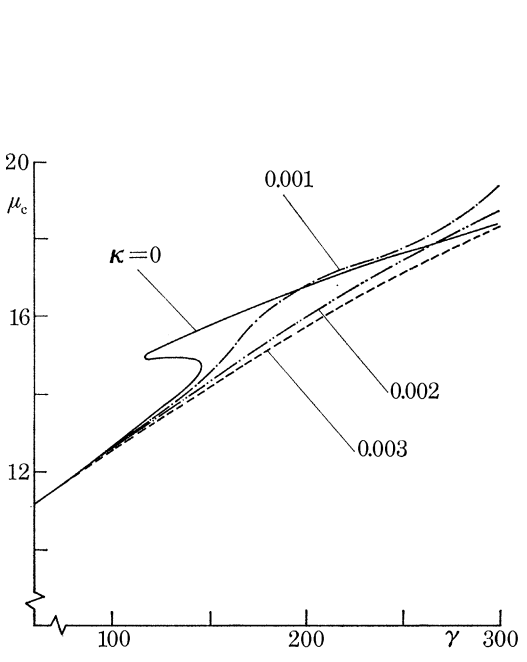

FIGURE 9

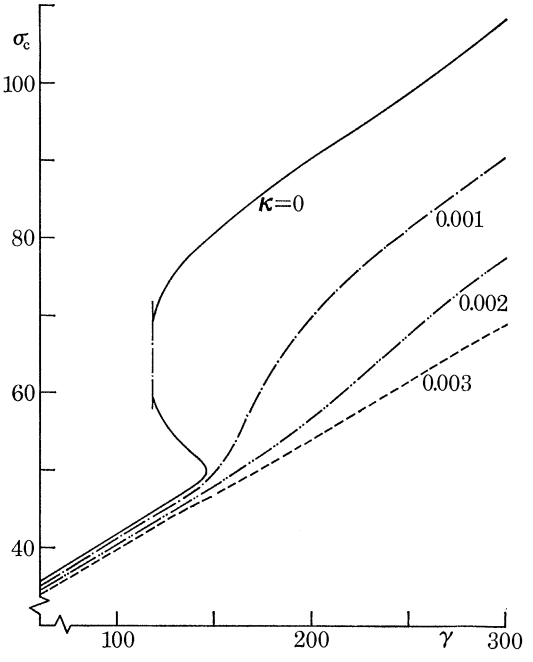

FIGURE 10

FIGURE 9. Effect of the weight parameter γ on the critical velocity μ_c for a range of values of the Kelvin damping parameter κ, when $\alpha = 1.0$; $\beta = 1.244$; $\eta = 0$.

FIGURE 10. Effect of the weight parameter γ on the critical frequency σ_c for a range of values of the Kelvin damping parameter κ, when $\alpha = 1.0$; $\beta = 1.244$; $\eta = 0$.

The calculated critical frequency σ_c is affected by Kelvin damping in a similar way as shown in figure 10. Now, however, intersection of the curves for the damped system with that for the undamped system seems unlikely and the critical frequency is reduced more at high values of γ than at low.

Figure 11 shows the calculated variation of μ_c and σ_c with κ for the particular values of $\alpha = 1.0$, $\beta = 1.244$ and $\gamma = 140$. (Viscous damping is again ignored so that $\eta = 0$.) Obviously the two curves are dependent to some extent on the particular values chosen for α, β and γ, but those

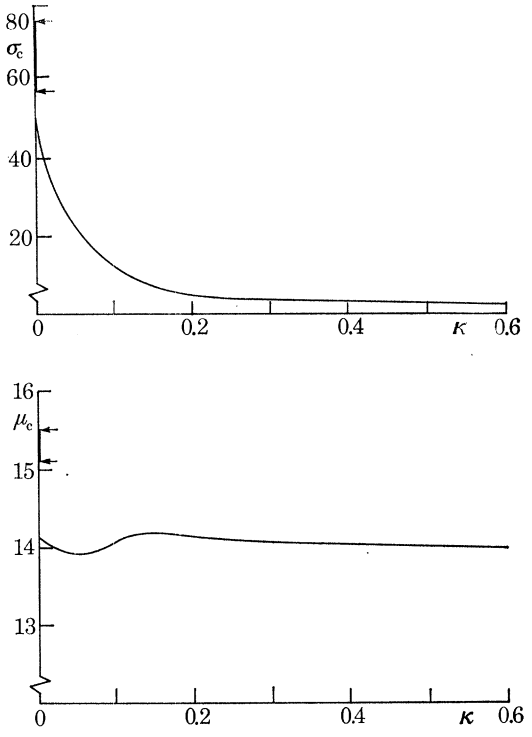

FIGURE 11. Variation of stability limits μ_c and σ_c with the Kelvin damping parameter κ, for $\alpha = 1.0$; $\beta = 1.244$; $\gamma = 140$; $\eta = 0$.

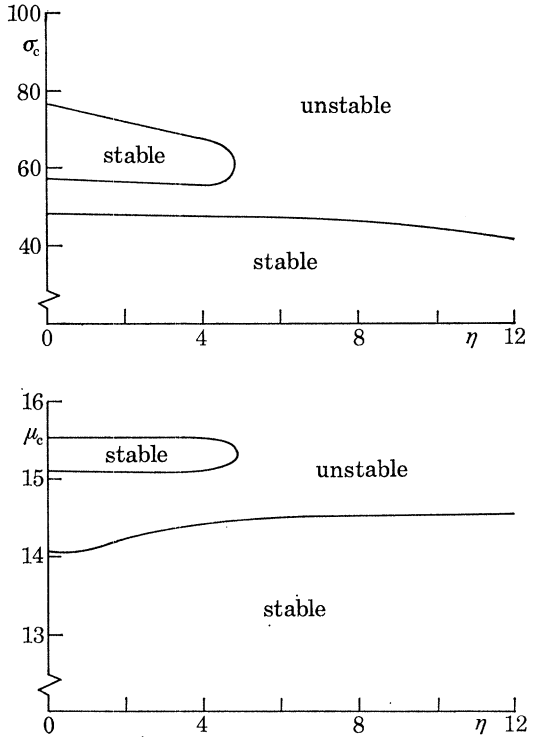

FIGURE 12. Variation of stability limits with the viscous damping parameter η, for $\alpha = 1.0$; $\beta = 1.244$; $\gamma = 140$; $\kappa = 0$.

values selected are of special interest as they place the system in the inflexion region described in the previous section and thus represent something of a 'worst case'. If α, β and γ are changed, the curves can be expected to be modified, but only quantitatively and not qualitatively. In short, figure 11 may be expected confidently to represent the effect of Kelvin damping with fair generality. We see that μ_c decreases at first and increases again over a certain range of κ after which it becomes almost constant. On the other hand, σ_c decreases significantly at first, as κ is increased. The second stable region, corresponding to the inflexion region for $\kappa = 0$, vanishes completely for the slightest value of κ. Its location is indicated by small arrows on the vertical axis.

Figure 12 shows the variation of μ_c and σ_c with viscous damping coefficient η. It is seen that the viscous damping raises the critical velocity slowly to a limiting value. Correspondingly, the critical frequency σ_c decreases very slowly with increase of η and the second stable region persists over a considerable range of viscous damping. It is of interest to compare the results contained in figures 11 and 12; it will be seen that the effects of Kelvin and viscous damping are quite different, particularly when the damping is small.

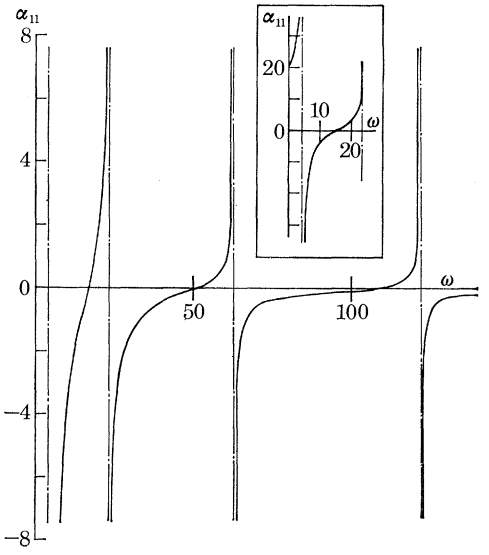

FIGURE 13. The direct receptance α_{11} as a function of frequency ω at zero velocity for $n = 4$; $\beta = 0.9$; $\gamma = 5$.

5. THEORY OF FORCED VIBRATION

5.1. *Direct receptance at the free end*

Figure 13 shows the variation of the direct receptance at the free end (i.e. α_{11}) with excitation frequency ω, for zero fluid velocity. Since $\mu = 0$, there is no hydrodynamic damping and so the tube behaves as a simple vertical beam clamped at its upper end, free at the lower one and forced to vibrate sinusoidally in a vertical plane. The receptance near the first natural frequency, in the range $0 < \omega < 20$, is shown inset.

Figures 14 (a)–(f) show curves of α_{11}, the direct receptance at lateral displacement of the free end of the tube for a series of values μ. In all cases, $\alpha = 3.0$, $\beta = 0.9$, $\gamma = 5$, while the value of μ

(which is constant for each diagram) is varied from $\mu = 1.0$ to $\mu = 8.0$. The critical values corresponding to these values are

$$\mu_c = \mu_{c1} = 2.749 \quad \text{for the first instability (in branch 2)}$$

$$\mu_c = \mu_{c2} = 6.728 \quad \text{for the second instability (in branch 4)}$$

and $\sigma_c = \sigma_{c1} = 15$ and $\sigma_c = \sigma_{c2} = 49$

respectively.

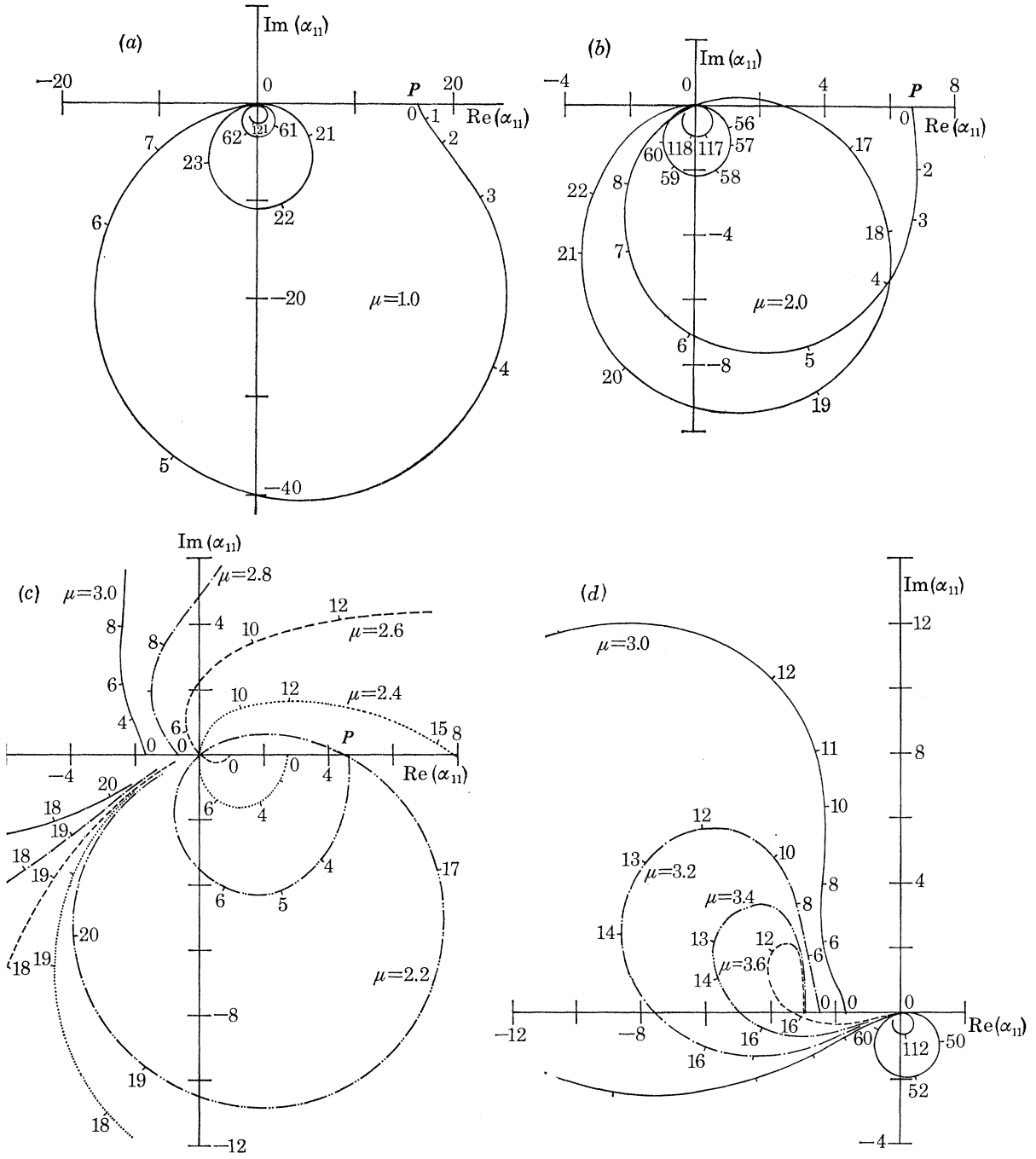

FIGURE 14 (*a–d*). For description see following page.

Fluid damping increases with the velocity† and the receptance diagrams change accordingly. With fluid velocities for which the system is stable, the receptance curves are basically circular loops superimposed on each other with different orientations. We shall therefore discuss only one curve in detail.

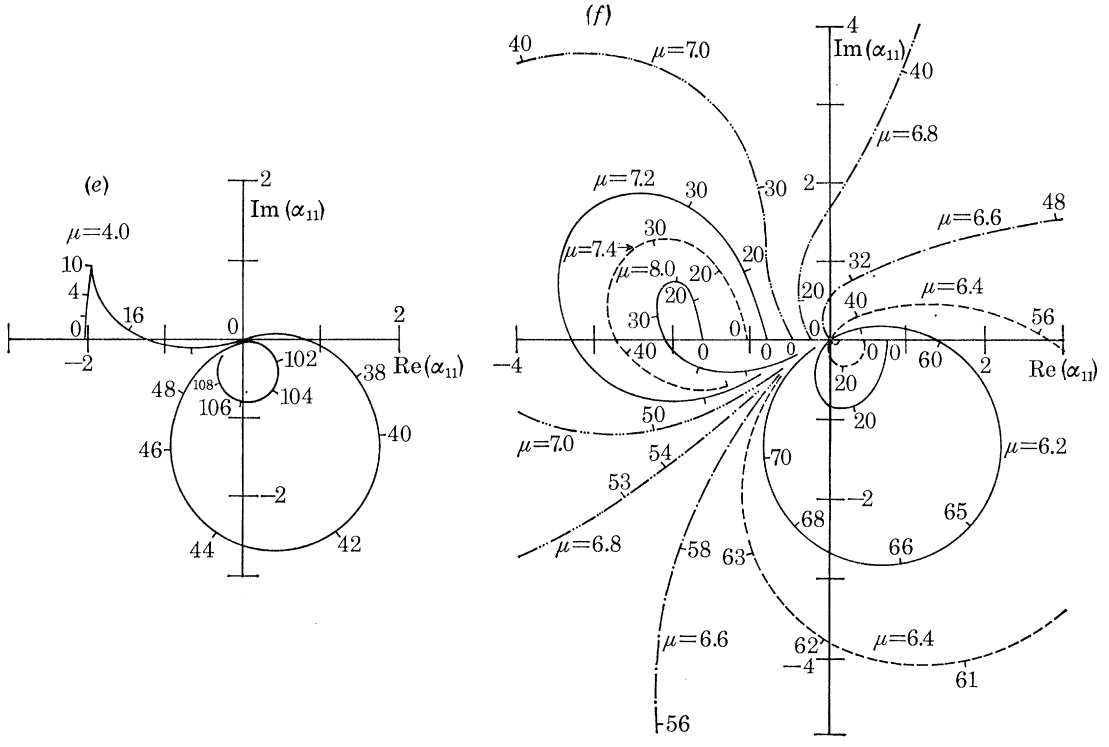

FIGURE 14. Variations of the dimensionless direct receptance α_{11} for a series of values of μ. Figures marked on the curves are values of dimensionless driving frequency ω. For all the curves

$$n = 4; \quad \alpha = 3.0; \quad \beta = 0.9; \quad \gamma = 5.$$

(*a*) $\mu = 1.0$,
(*b*) $\mu = 2.0$,
(*c*) $\mu = 2.2, 2.4, 2.6, 2.8, 3.0$,
(*d*) $\mu = 3.0, 3.2, 3.4, 3.6$,
(*e*) $\mu = 4.0$,
(*f*) $\mu = 6.2, 6.4, 6.6, 6.8, 7.0, 7.2, 7.4, 8.0$.

Figure 14 (*b*), for instance, shows the receptance variation with frequency at $\mu = 2.0$. The curve starts at a point P on the positive real axis, the in-phase axis, at $\omega = 0$. As the frequency ω increases the curve develops in the lower half of the plane, forming four circular loops, in the last of which the receptance tends to zero as the frequency increases to infinity. The four circular loops correspond to the four bending degrees of freedom used in the analysis. The eigenvalues of the system at $\mu = 2.0$, obtained as the roots of the characteristic equation found by putting $F = 0$ in equation (46), are $(-2.28 \pm 5.46i)$, $(-1.41 \pm 19.19i)$, $(-1.77 \pm 58.22i)$ and $(-1.74 \pm 117.58i)$.

Two arcs of the circular loops‡ of figure 14 (*b*) are shown enlarged in figure 15. They are the arcs in the vicinity of the 'hydrodynamically damped' natural frequencies $\omega = 5.64$ and 19.19.

† Unless otherwise stated the word 'damping' will now refer to hydrodynamic damping only.
‡ The other two loops exhibited the same feature. They are omitted for the sake of clarity.

The excitation frequency is marked in equal increments and the damped natural frequencies are located by interpolation. We notice in these figures that the frequency gradient along the receptance curve reaches its minimum at each of these damped natural frequencies. This behaviour is somewhat analogous to that discussed by Kennedy & Pancu (1947) and by Bishop & Gladwell (1963) for linear *passive* systems. The 'resonance diameter' is not parallel to the imaginary axis (as it would be for a passive system). This is demonstrated by the lines indicating the direction normal to the receptance curve at the damped natural frequencies in the figure.

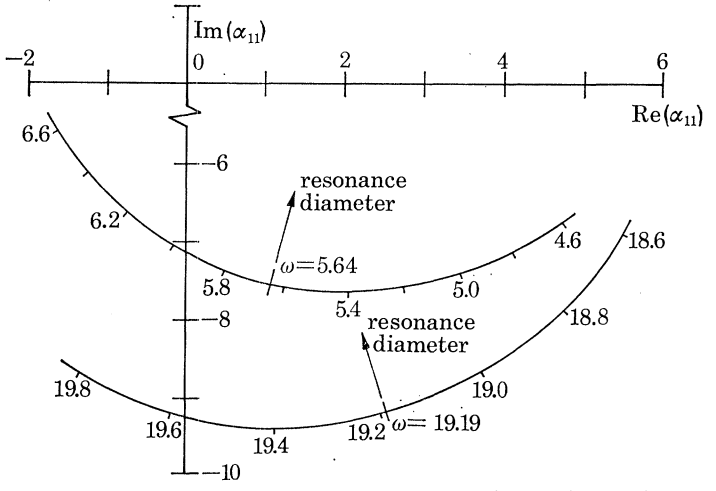

FIGURE 15. Variation of the dimensionless direct receptance α_{11} near first and second resonances in figure 14 (*b*). Figures marked on the curves are values of ω.

Returning to figure 14 (*b*), we notice that the value $\mu = 2.0$ is well below the instability boundary of the system so that the tube is effectively a dynamic system with heavy hydrodynamic damping. Nevertheless there are two other features of the receptance diagrams that are worthy of note. First it will be seen that the receptance vanishes almost completely at certain frequencies between the resonant values. Secondly it will be observed that parts of the receptance loops lie above the real axis. Neither of these aspects would be expected with a passive system; with them, the receptance vanishes only at infinite frequency when there is heavy damping and, further, phase leads are not encountered because it implies that the system can do work. These two observations will be discussed later.

At higher velocities the system becomes incipiently unstable. Figures 14 (*b*) and (*c*) show that as μ increases the point P where the receptance curve starts on the positive real axis moves closer to the origin indicating that the static lateral stiffness increases. We also see that the first loop diminishes in size while the second expands remarkably. (It was found that instability first occurs in the second branch of the roots locus diagram.) Figure 14 (*c*) shows clearly that as μ approaches the first critical value ($\mu_{c1} = 2.749$) the second loop continues expanding until it becomes of infinite diameter at the critical velocity. At higher velocities still the first loop becomes difficult to identify and the second loop appears in the second quadrant of the complex plane instead of the fourth, as seen in figure 14 (*d*). With further progressive increases of μ the second mode loop, still in the second quadrant, diminishes gradually until it, too, eventually disappears. (See figure 14 (*e*).)

For this range of μ (i.e. $\mu < 5$) the third and fourth loops continue to appear much as they would for a passive damped system. The third and fourth branches in the roots locus (which predominantly account for those loops) were found to lie in the left hand side of the diagram.

Every point of a receptance diagram represents the sum of the responses in all the modes. It has been noted that this sum may be such that the curve intersects the positive real axis, as in figure 14 (*b*) for example; at the frequency corresponding to such an intersection, no work is done by the driving force. In figures 14 (*d*) and (*e*) there is an intersection with the negative real axis and this has a different interpretation, for in these diagrams mode 2 has become unstable. The intersection occurs in each case at the characteristic frequency of this unstable mode since no work has to be done to maintain the oscillation.

At higher velocities, in the unstable region, the receptance curves look roughly similar to those in the stable region, but with the first and second loops now entirely absent. Each loop present may still be associated with the response in a 'mode' of vibration.

On approaching the second critical velocity, $\mu_{c_2} = 6.728$, the third and fourth mode loops now behave in a similar way to the first and second near the first critical value. Thus figure 14 (*f*) is similar to 14 (*c*) and the same state of affairs as before arises.

Qualitatively speaking, the same behaviour is observed at both of the two critical velocities. The curves of direct receptance start near the origin (implying that the lateral stiffness is very large) and shoot off to infinity through the first quadrant above the real axis as the excitation frequency increases. (An infinite value of the lateral stiffness is not feasible, however, and this point will be discussed in more detail later.) Passage to infinity through the first quadrant seems reasonable on physical grounds. At the critical velocity, the tube tends to oscillate with its critical frequency. When the excitation frequency is less than the critical, energy flows from the tube to the driving mechanism and the displacement therefore leads the excitation and causes the receptance curve to lie above the real axis. The phase lead continues until the excitation frequency reaches the critical value where the amplitude becomes infinite. At this critical frequency, the forcing mechanism neither absorbs energy nor supplies it since all the energy supplied to the tube is provided solely by the fluid. Beyond the critical frequency the tube is forced to oscillate more rapidly and the displacement lags behind the force, i.e. the receptance curve appears below the real axis.

5.2. *Inverse receptance at the free end*

Figures 16 (*a*)–(*d*) show the inverse receptance at the free end, i.e. $1/\alpha_{11}$, for $\mu = 2.0, 2.4, 2.6$ and 3.0 respectively. These values of velocity are around the first critical value, and we see that the curves are for the most part nearly straight lines. With the exception of the first, corresponding to the smallest values of ω, these lines lie almost parallel to the real axis. The remarkable rotation of the line corresponding to inversion of the first receptance loop is due to the change in location of the first modal circle relative to the origin of the receptance diagram. The appearance of straight lines in the inverse receptance diagrams is due to the fact that the receptance circles pass through, or very near to, the origin.

The behaviour of the inverse receptance near the instability boundary is shown separately in figure 17 (*a*). Only the range close to the critical velocity and critical frequency is shown. The dotted line connects the second characteristic frequency at each fluid velocity. It is seen that for velocities lower than μ_{c_1} the inverse receptance curve intersects the positive real axis and proceeds in the direction of increasing phase angle, the origin lying on the left hand side of the curve. As the velocity approaches μ_{c_1} the curve shifts nearer to the origin until it passes through it at the

critical velocity and the critical frequency. For velocities higher than μ_{c1} the curve is shifted further to the left where it intersects the negative real axis and proceeds in the direction of decreasing phase difference, the origin now appearing on its right hand side.

At any higher value of μ, the higher modes which are still stable repeat the behaviour of the lowest modes at the velocities lower than the critical until the second critical velocity is approached. Figure 17 (b) shows the inverse receptance around the second critical velocity. The behaviour is quite similar to that in the vicinity of the first critical value.

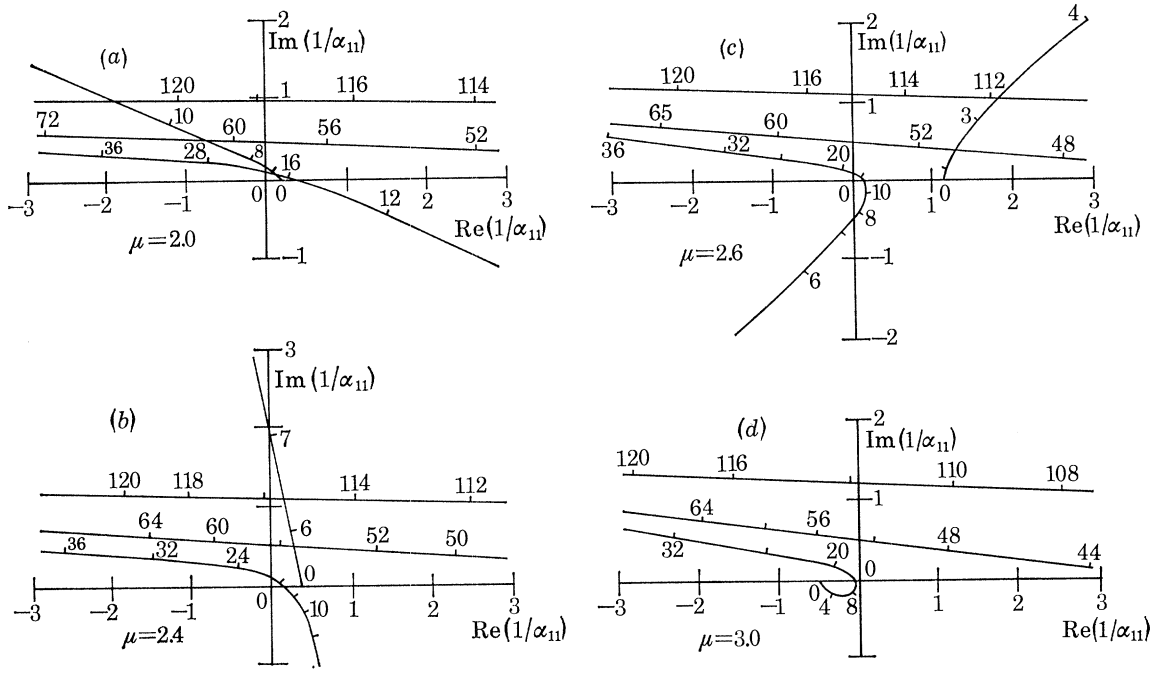

FIGURE 16. Inverse dimensionless receptance $1/\alpha_{11}$ for a range of values of μ. Figures marked on the curves are values of ω. The curves correspond to those of figure 4. (a) $\mu = 2.0$, (b) $\mu = 2.4$, (c) $\mu = 2.6$, (d) $\mu = 3.0$.

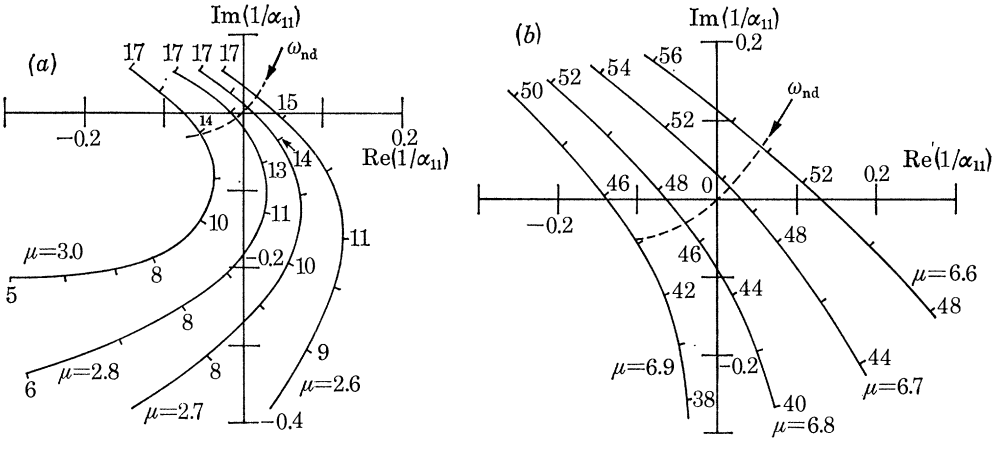

FIGURE 17. Variation of dimensionless inverse receptance $1/\alpha_{11}$ at a stability boundary. Figures marked on the curves are values of ω. (a) first instability boundary, (b) second instability boundary.

Results in figures 17 (*a*) and (*b*) confirm the 'shifting rule' established earlier, namely, the flutter instability boundary is characterized by the passage of the inverse receptance curve through the origin exactly at the critical velocity and the critical frequency.

5.3. *Special features of the receptance curves*

In presenting the computed results for the system of figure 3 we pointed out a number of features of general validity. We come now to discuss certain remaining points that appear either to be peculiar to the system in question or to warrant special attention. These are:

(1) the vanishing of the receptance at finite frequency,

(2) the appearance of the receptance curve above the real axis when the system is completely stable,

(3) the migration of the starting point of the receptance curve along the real axis near the origin.

The first point suggests that the system may have some pure imaginary anti-resonance eigenvalues. As pointed out earlier these are the (resonance) eigenvalues of the system that results when the excitation point is constrained to zero displacement – that is to say when the tube is clamped-pinned.

The analysis of the clamped-pinned tube is outlined briefly in the appendix. The roots locus diagram, for the same values of α, β and γ, is shown in figure 18. The four branches of the clamped-pinned tube climb down the imaginary axis as the velocity increases and each branch in turn splits at the origin of the diagram into two pure real branches which sweep along the positive and negative axes. Figure 18 therefore does confirm that all the anti-resonance eigenvalues are pure imaginary up to some value of μ, beyond which one or more becomes pure real with positive and negative real values. Before divergent instability is reached the clamped-pinned tube has pure imaginary eigenvalues. Thus there is no hydrodynamic damping of the tube motion. The modes of free vibration of the clamped-pinned tube are therefore exactly in phase or exactly out of phase.

This behaviour of the clamped-pinned tube throws some light on the dynamic behaviour of the clamped-free tube near the anti-resonance frequency. At such a frequency the free tube vibrates under the action of an external force at its lower end, and it does so in the manner of free vibration of the clamped-pinned tube. It was in fact verified that the frequencies at which the receptance tends to zero coincide with the natural frequencies of the clamped-pinned tube as extracted from its roots locus diagram. In addition when the free tube was excited at 0.4 of its length from the top (i.e. at $Z = 0.4$) the receptance did not vanish as before. This is seen easily when figure 19 is compared with figure 14 (*b*).

The second feature, namely the appearance of some parts of the receptance curve above the real axis, may be connected with the first. We have seen that there is no damping at an anti-resonance frequency (equal to a natural frequency of the equivalent clamped-pinned tube) and the vibration modes are either exactly in phase or exactly out of phase. As the excitation frequency is increased the tube departs from the anti-resonance state and damping builds up gradually. It seems possible that the phase lead that is sometimes observed is related to the variation of damping. The phase lead does not appear in figure 19 when there is no anti-resonance.

We turn now to the third feature, namely the movement of the starting point of the receptance curve along the real axis back and forth through the origin as the velocity increases. The natural frequencies of the system were found to decrease in general at higher velocities, as may be seen from the roots locus diagram, so it might be concluded that the stiffness of the system decreases

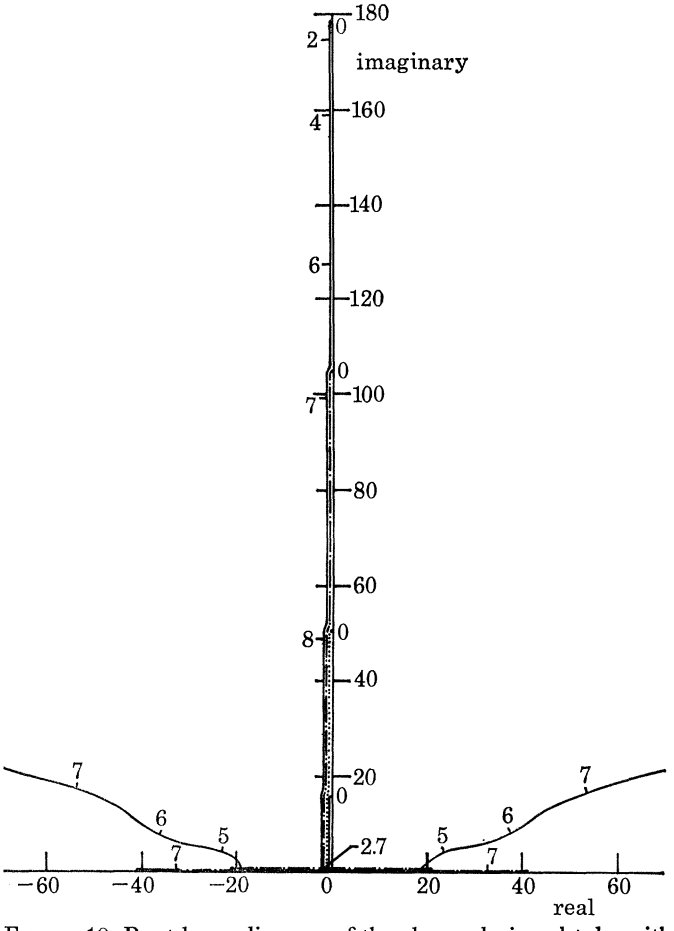

FIGURE 18. Root locus diagram of the clamped-pinned tube with $n = 4$; $\alpha = 3$; $\beta = 0.9$; $\gamma = 5$.

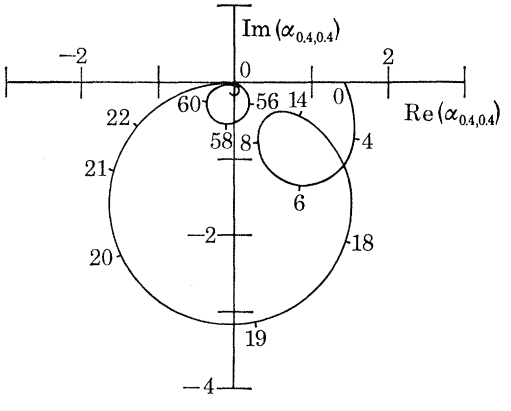

FIGURE 19. Dimensionless direct receptance at $X = 0.4$ for $\mu = 2.0$ with $n = 4$; $\alpha = 3$; $\beta = 0.9$; $\gamma = 5$. Figures marked on the curve are values of ω.

as well since the equivalent mass does not change. This conclusion is in conflict with the movement of the point P in figure 14 nearer to the origin; for that movement indicates higher lateral stiffness with higher velocities until the stiffness reaches an infinite value when the point P lies exactly at the origin. We notice, however, that the point P lies at the origin when $\mu \approx 2.7$ (see figure 14 (c)). This value of μ is the first divergence boundary of the corresponding clamped-pinned tube as seen in figure 18, and this suggests a reasonable explanation for the behaviour. In the vicinity of a divergence instability boundary the forced clamped-free tube, behaving as if it is clamped-pinned, tends to buckle continuously in one direction. Consequently a large force is required to hold the free end in position. At velocities higher than the divergence boundary the tendency to buckle will cause the tube to press against the support, causing the displacement to be exactly out of phase with the applied force so that the point P appears on the negative part of the real axis.

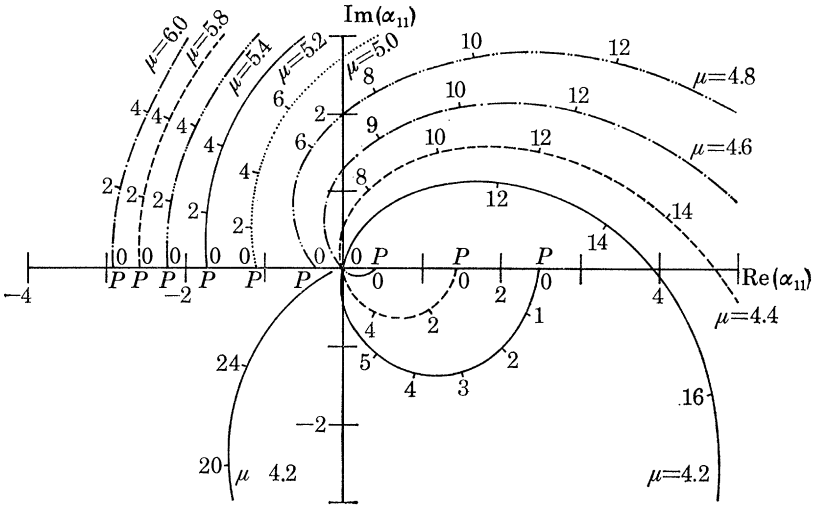

FIGURE 20. Variation of dimensionless direct receptance α_{11} at the divergence limit and flutter limit for a tube in which $n = 4$, $\alpha = 1$, $\beta = 0.9$, $\gamma = 5$, $\eta = 0$, $\kappa = 0$. Figures marked on the curve are values of ω.

The migration of the point P is not related to the flutter boundary which happened to occur near the divergence boundary for the clamped-pinned tube. To clarify this point a different case is considered in which $n = 4$, $\alpha = 1.0$, $\beta = 0.9$ and $\gamma = 5$. At these values a clamped-free tube has a flutter boundary when $\mu = 6.07$ while a clamped-pinned tube first diverges when $\mu = 4.74$. The receptance diagram for the clamped-free tube in this range of velocity is shown in figure 20. It is seen that the point P passes through the origin between $\mu = 4.6$ and $\mu = 4.8$ while near $\mu = 6.07$ no particular changes occur at the starting point of the receptance diagram.

To sum up, we see that the apparently strange features in the receptance of the clamped-free tube are in fact explicable by reference to the anti-resonance eigenvalues; that is, in terms of the corresponding clamped-pinned tube. We find a sort of 'dynamic interference' between the parameters of the clamped-pinned tube (like its divergence limit) and those of the clamped-free tube, under harmonic excitation.

6. EXPERIMENTS

6.1. *General remarks and apparatus*

Free oscillation tests were performed to determine the instability boundary, first using a constant tube length with different nozzles and secondly using a selected nozzle with different tube

lengths. This meant changing α at constant γ and vice versa. It was not necessary to use tubes of various cross sections or various fluids since the loading parameter β has been sufficiently investigated before by Gregory & Paidoussis (1966) and Paidoussis (1970). Thus only one fluid – water – was used and various sizes of tubes were tried until a suitable one was found; the chosen size was such as to give $\beta = 1.244$.

Forced vibration experiments were performed to investigate the receptance and its inverse. Since the direct receptance increases to infinity and its inverse decreases to zero at the instability boundary, it was more convenient to measure the latter. The inverse receptance was measured in a straightforward manner. A lateral sinusoidal displacement of constant amplitude was imposed on the tube. The necessary applied force at the point of excitation was therefore proportional to the inverse of the direct receptance at that point. By measuring the amplitude and phase of the applied force, the inverse receptance could be completely determined.

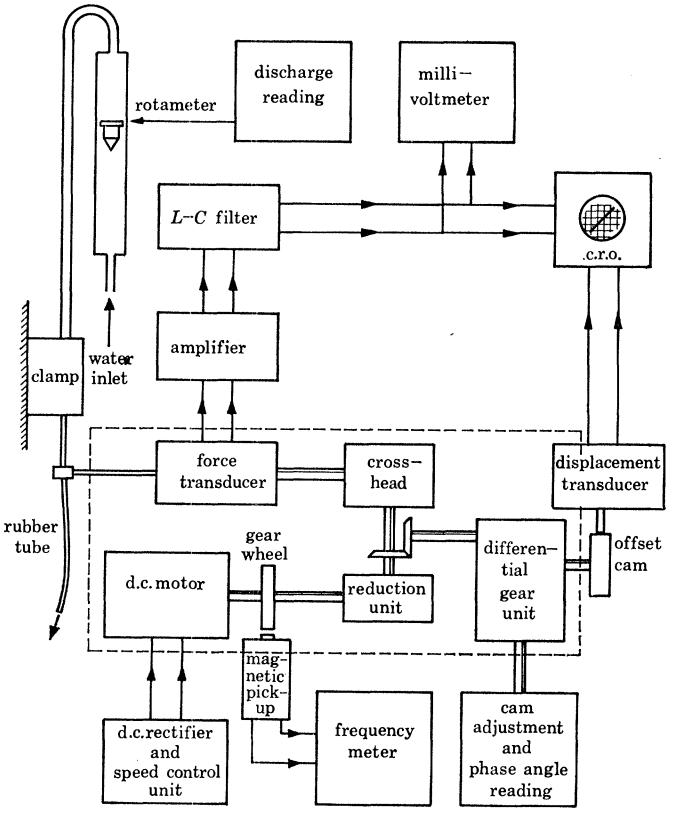

FIGURE 21. Diagrammatic layout of apparatus.

The tubes were made of high quality surgical silicon rubber and were carefully selected so that defects were avoided. Since they were not specially cast, however, the rubber tubes all had a slight bend. The upper end of each rubber tube used in the experiments was shrunk inside a metal pipe whose bore just fitted the outside diameter of the tube. The pipe was clamped firmly between two metal Vee blocks mounted on a rigid frame. High pressure water was supplied to the tube through a regulator and the rate of flow was measured with a rotameter. A flow straightener was fitted just before the entry to the tube. The nozzle was a Perspex disk whose diameter was slightly larger than the internal tube diameter. A central hole was drilled in the disk so as to give the desired value of α and the disk was then shrunk inside the tube at its free end.

A cross-head mechanism, based on the Scotch-yoke principle, was used to impose the sinusoidal lateral vibration on the tube. The cross-head was driven by a d.c. motor through a speed reduction unit, a speed-control unit being incorporated with the d.c. rectifier feeding the motor. The force between the tube and the cross-head was monitored by a force transducer.

The shaft driving the cross-head also drove a sinusoidal cam at the same speed, but it did so through a differential gear unit of speed ratio 1 : 1. This cam actuated a displacement transducer that generated a sinusoidal signal of the same frequency as the movement of the cross-head. But the casing of the differential unit was capable of independent rotation about its axis so the phase of the displacement transducer signal could be advanced or retarded with respect to the force transducer signal. This was achieved without affecting the speed ratio between the cross-head shaft and the cam.

A diagrammatic layout of the apparatus is shown in figure 21. Electrical connections are indicated by single lines. Mechanical connections are represented by double solid lines. The dotted rectangle refers to a common base which carried the motor, the speed reduction unit, the cross-head and the differential unit.

6.2. *Procedure and measurements*

Neither the experimental procedure nor the manner of taking measurements required sophisticated equipment. The tube length could be varied between 25 and 60 cm and its value was directly measured. The outside diameter was measured at different places and in different directions by means of a micrometer and an average value was taken. The inside diameter was measured indirectly by weighing a known length of the tube with and without water inside it. By this means the mass of tube and mass of water per unit length were also determined. The value of the Young modulus was found by applying simple tension and compression tests on suitable specimen lengths of the tube and evaluating the average slope of the force-deflexion curve. The value of the flexural rigidity EI was checked by measuring the natural frequency of the empty tube when vibrating freely as a vertical cantilever. Further details are given elsewhere (Wahed 1969).

The experimental procedure for free oscillation was very simple. The water flow was increased in small steps and care was taken to allow conditions to become steady at each. When the tube started spontaneous oscillation the rate of water discharge was recorded and thence the critical water velocity μ_c determined. The critical frequency σ_c was obtained by observing the sustained oscillations.

To measure the force acting on the tube in forced vibration experiments a force transducer was fixed in the link between the cross-head and the tube. It was basically a flexible bimetallic strip with four strain gauges on its faces. A low frequency millivoltmeter was used to measure the r.m.s. value of the amplified filtered force signal. The signal was also fed into a long persistence cathode ray oscilloscope to control the vertical deflexion of its electron beam.

The displacement transducer generated a reference sinusoidal signal of the same frequency as the cross-head movement. This signal was fed into the same oscilloscope, controlling the horizontal deflexion of the electron beam. As already mentioned the phase of this signal could be changed by rotating the differential gear unit transmitting motion to the cam. This adjustment was made manually and a protractor scale, whose zero indicated the in-phase position, indicated the amount of rotation. In general the two signals produced an ellipse on the oscilloscope screen. The differential gear was then rotated until this ellipse was reduced to a straight line. The pro-

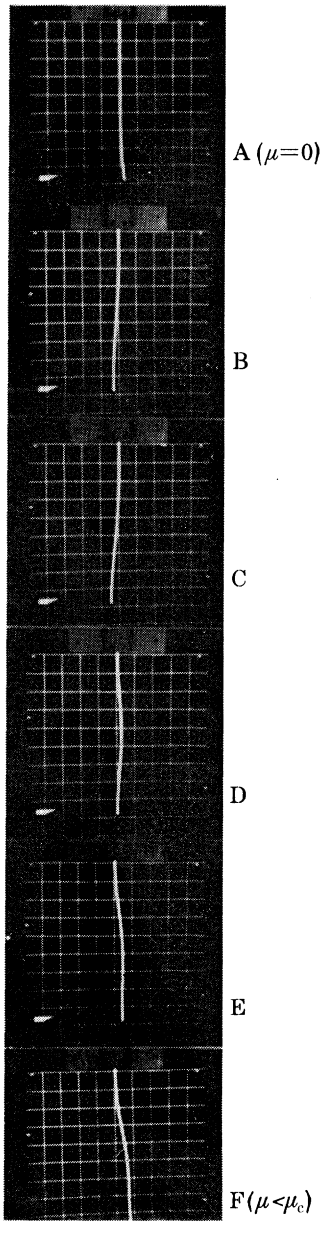

FIGURE 22.

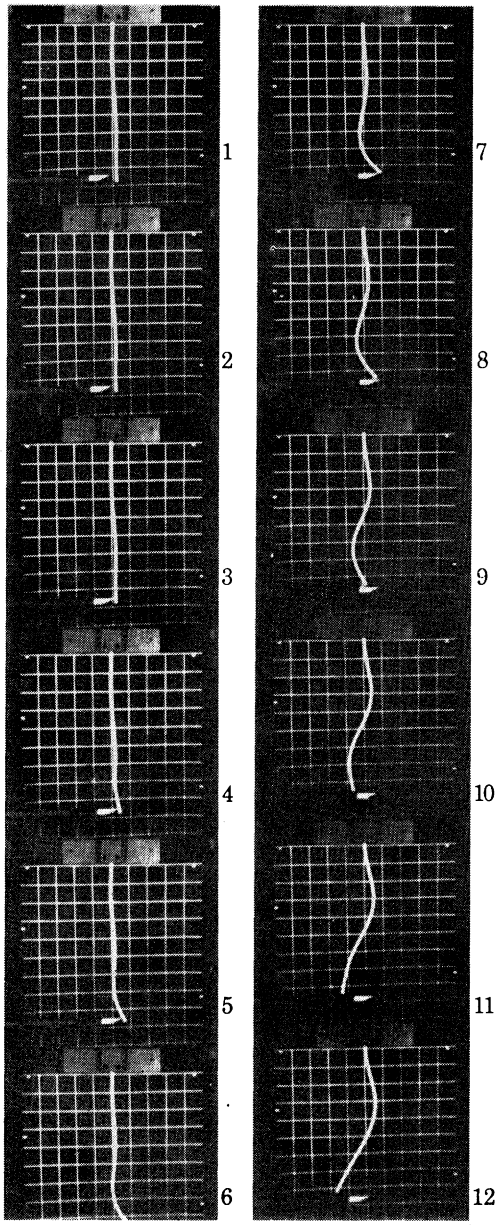

FIGURE 23.

FIGURE 22. Static distortion shapes before instability.

FIGURE 23. Dynamic instability after touching the free end of the tube.

(*Facing p.* 34)

PHILOSOPHICAL TRANSACTIONS OF THE ROYAL SOCIETY A MATHEMATICAL, PHYSICAL & ENGINEERING SCIENCES

tractor reading then gave the phase angle between the two signals, i.e. between the force and the displacement.

A magnetic pick-up was placed so as to face the teeth of a toothed wheel rigidly keyed on the motor shaft. Movement of the teeth opposite the magnetic pick-up generated electric pulses that were fed into a digital frequency-meter. In this way the speed of the motor, and consequently the frequency of oscillation, was measured.

The general procedure adopted in forced vibration experiments was to fix the water velocity at a suitable value and then to change the frequency of excitation, i.e. the motor speed, gradually. At each frequency of excitation the two signals fed to the oscilloscope were made to produce a line on the screen by rotating the differential gear unit against the protractor scale. When this had been done the readings of rotameter, frequency meter, millivoltmeter and protractor scale were recorded. These readings gave the water velocity, the excitation frequency, the force amplitude and the phase angle respectively.

In plotting the results, the readings from some instruments have been used directly since they vary proportionally to the parameter of interest. The frequency factor f, for example, was the reading on the frequency meter. This was equal to 480 times the frequency of oscillation in Hz because the toothed wheel facing the magnetic pickup had 480 teeth and the frequency meter displayed the number of pulses per second. Similarly the discharge reading R was used instead of the velocity parameter μ employed hitherto. (The setting of the rotameter scale was in fact such that the flow velocity U was related to R by the equation $U = 1.185R \times 10^{-6}/A\ \mathrm{m\,s^{-1}}$, where A is the internal area of cross section in square metres.)

The amplitude of sinusoidal movement of the cross-head was maintained at 2.0 mm. The force corresponding to the reading of the millivoltmeter was obtained by direct calibration under dynamic conditions. The scale of the inverse receptance is shown in the diagrams.

7. Free vibration experiments

7.1. *Static distortion*

As the water velocity was gradually increased the tube was noticed to distort slowly into different shapes successively. This phenomenon was observed in all the experiments. These shapes differed from the distortions due to residual internal stresses in the rubber; for when a distortion of the latter type was present, it appeared merely as an irregular shape localized at some section of the tube only.

The observed shapes were similar to the lowest buckling modes of a simple Euler beam under compression and photographs of them are shown in figure 22, plate 1. The first and second modes of a uniform strut, and also the transition from the first to the second, were easily observed in all the experiments. The third, and sometimes the fourth, appeared only with long tubes. Having become distorted the tube remained in equilibrium in its deflected configuration. Any transient disturbance, whether lateral or longitudinal, died out and the tube retained the same distorted shape until the water velocity was increased sufficiently to cause flutter instability.

This process of distortion was of an essentially static nature and it was not an instability by divergence. Had the distortion been divergent, it would have grown continuously, neither acquiring equilibrium nor changing its configuration. Moreover the deflexion at this configuration was too small to be attributed to nonlinear effects.

The static nature of this observed distortion became even more apparent when it was compared with the actual dynamic instability by divergence that occurred when the free end of the tube was touched. The tube deflexion then grew unidirectionally, and continued to do so even after an extremely large deflexion had been achieved. This is illustrated in figure 23, plate 1, which shows a series of ciné photographs taken immediately after the lower end of the tube was touched with the tapered stick appearing in the photographs.

It will be recalled that the equilibrium configuration of a cantilever beam under a follower compressive force at its free end is not yet known since the usual differential equation fails to give any solution but the trivial one. Evidently this does not necessarily mean that an equilibrium configuration does not exist. We shall return to this point later.

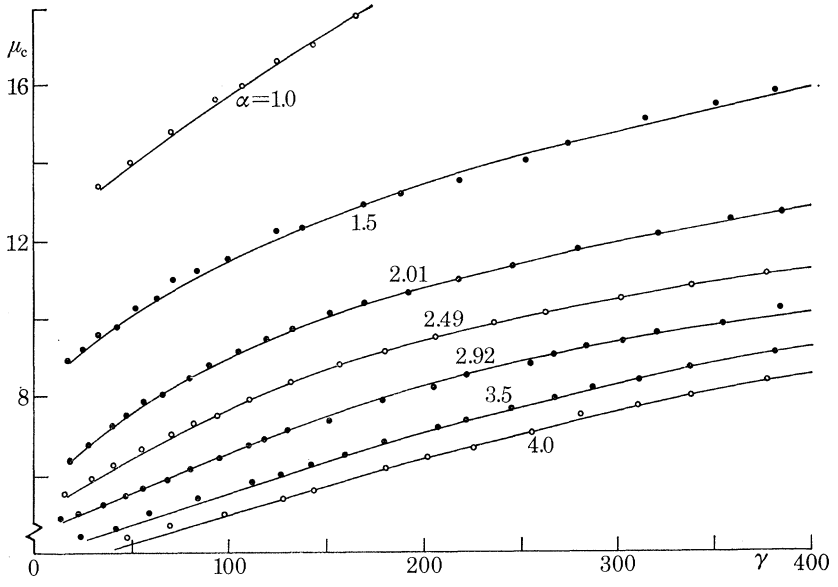

FIGURE 24. Variation of critical velocity μ_c with the weight parameter γ for a range of values of the nozzle parameter α, for $\beta = 1.244$.

7.2. *Experimental results*

Results of the experiments carried out to determine the variation of the critical velocity μ_c and critical frequency σ_c with the nozzle parameter α and the weight parameter γ are shown in figures 24 and 25. The effect of varying the parameter α was investigated by considering two sets of nozzles. In the first set α varied from 1.0 to 1.5 with small increments; this covered the more interesting range as revealed by the theory in § 4 (see figure 7). The second set included a coarser range, up to $\alpha = 4.0$. The results shown in these figures are self-explanatory. They show good qualitative agreement with the theory. In particular it will be seen that as α is increased, μ_c decreases greatly and σ_c is only affected relatively slightly.

Figures 26–28 show some experimental results with corresponding theoretical calculations for values of κ chosen on the basis of free vibration tests. These figures show that the experimental results are generally higher than the theoretical values. There is a difference of about 15 % in μ_c and about 6 % in σ_c on average and the difference is more or less uniform. This indicates that the rate of change of μ_c or σ_c with γ or α is more or less the same in theory as in the experiment.

The reason for the difference referred to is perhaps the static distortion of the tube before the instability boundary was reached. Displacement from equilibrium to the deflected shape absorbs some of the input energy, the amount being determined by the elastic properties of the tube. The instability boundary, which is effectively determined under the assumption of a balance between input energy and output dissipative energy, is therefore reached at a higher velocity than would have been the case without buckling. The theoretical analysis of free vibration does not take into account this effect of static distortion and hence it predicts a lower instability boundary.

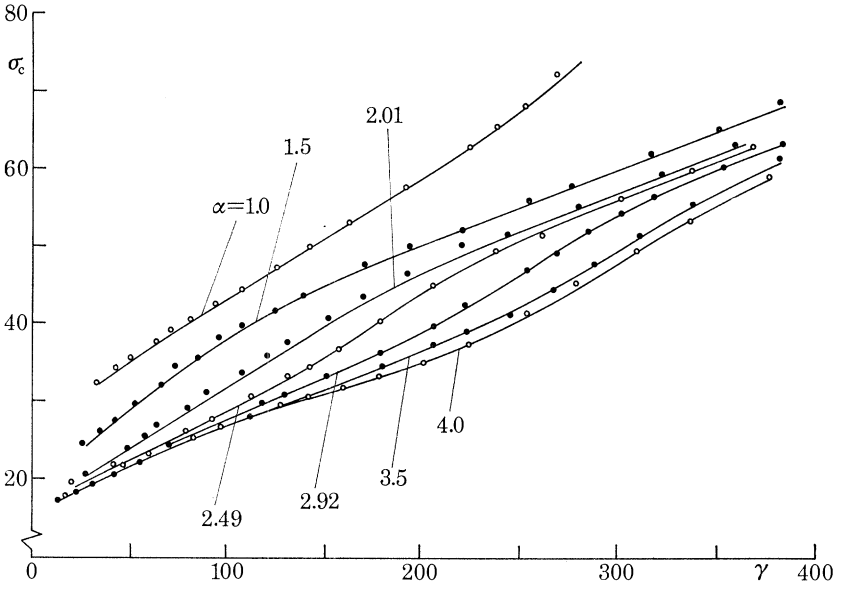

FIGURE 25. Variation of critical frequency σ_c with weight parameter γ for a range of values of nozzle parameter α, when $\beta = 1.244$.

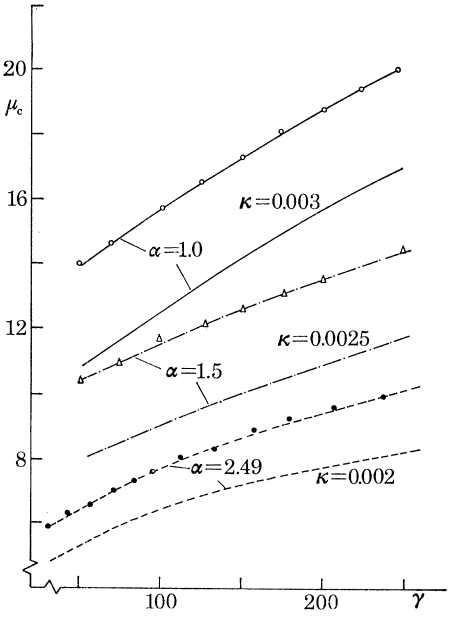

FIGURE 26. Variation of experimental and theoretical values of the critical velocity μ_c with the weight parameter γ for a range of α and for assumed values of κ when $\beta = 1.244$ and assuming that $\eta = 0$.

PHILOSOPHICAL TRANSACTIONS OF THE ROYAL SOCIETY A MATHEMATICAL, PHYSICAL & ENGINEERING SCIENCES

Evaluation of the strain energy absorbed in static distortion requires the determination of the equilibrium configuration of the tube as a cantilever beam under a follower compressive force. Bolotin (1964) refers to a similar situation in connection with the stability of a straight equilibrium configuration under a compressive follower force and states (on pages 289–290) that: 'Of special importance is the fact that the transition from real to complex roots can proceed through multiple values which are different from zero, i.e. by passing through neutral equilibrium.'

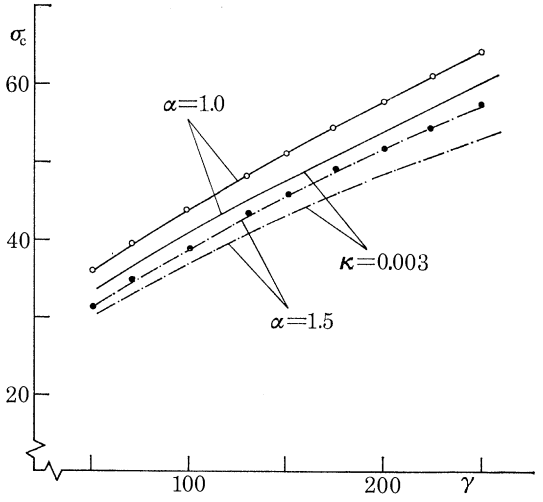

FIGURE 27. Variation of experimental and theoretical values of the critical frequency σ_c with weight parameter γ, when $\beta = 1.244$ and it is assumed that $\eta = 0$.

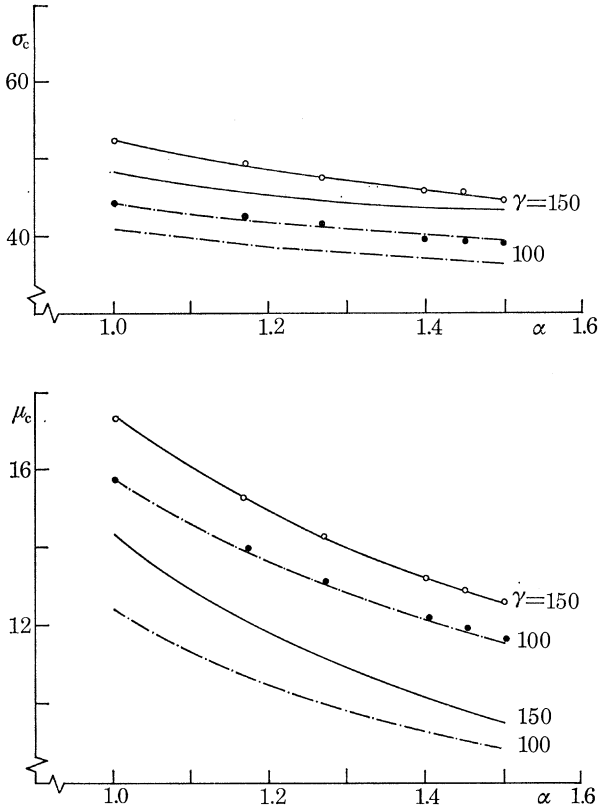

FIGURE 28. Variation of experimental and theoretical stability limits with nozzle parameter α, for $\beta = 1.244$; $\kappa = 0.003$; $\eta = 0$.

Other reasons for the deviation between the experiments and the theory may be due to the lack of initial straightness of the tube and nonlinearities in the system. Their contribution, however, is expected to be only small compared with that of the static distortion effect.

8. Forced vibration experiments

8.1. *Practical considerations*

Limitations had to be accepted on the range of parameters that would be employed in the forced vibration experiments. Very low excitation frequency made it difficult to obtain reliable and consistent readings. Again, very high water velocity made the tube vibrate significantly without reference to the driving mechanism.

The horizontal level below the clamped end of the tube at which the lateral excitation was imposed (i.e. the value of Z) was decided after some preliminary trials. The level at which the driving force is applied influences the extent to which each separate mode is excited. Thus if the excitation point coincides with a node of one particular mode, it is unlikely that this mode will be excited at all.

It was noticed that in the vicinity of the instability boundary the tube was very sensitive to anything touching the free end. As mentioned before, this caused the tube to distort in one direction like a clamped-pinned tube that is unstable in divergence. When this happened, it was extremely difficult to arrest the tube, let alone to oscillate it sinusoidally. It was therefore decided to excite the tube at a point nearer its clamped end. Unfortunately, this decision did not remove this particular difficulty completely since the portion of the tube below the excitation point behaved as a pinned-free beam on its own. This behaviour was most pronounced near a natural frequency of the lower part when it acted as such a beam. The amplitude of movement at the lower free end was then large, as was the amplitude of force at the excitation point. It was also noticed that the phenomenon of beating was also observable near the instability boundary; this probably represented some interaction between the excitation frequency and the natural frequency of the lower part of the tube. No steady readings could be obtained when beating occurred.

Numerous attempts were made to excite the tube, a number of sections being chosen for the imposition of the sinusoidal displacement. It was also found necessary to adjust the amplitude of the imposed displacement. Satisfactory results were eventually obtained but it has to be said that the study of a resonance test on an active system near an instability boundary is not easy.

8.2. *Force response with zero flow velocity*

A set of preliminary experiments was carried out in order to investigate the dynamics of the vertical tube and the effects of small water velocities. This was necessary because familiarity with the force response locus was needed before the instability boundary could be explored with adequate comprehension.

Figure 29 (*a*) shows the force loci for stationary fluid inside the tube ($R = 0$) and for a range of small water velocities (up to $R = 12$). The level at which the excitation was applied is $Z = 0.3$. Figure 29 (*b*) shows the corresponding results for $Z = 0.4$. In this figure, and all the rest of the figures that follow, the displacement vector is taken to coincide with the positive real axis, which is therefore referred to as the 'in-phase axis'. The response curves are plotted above the real axis,

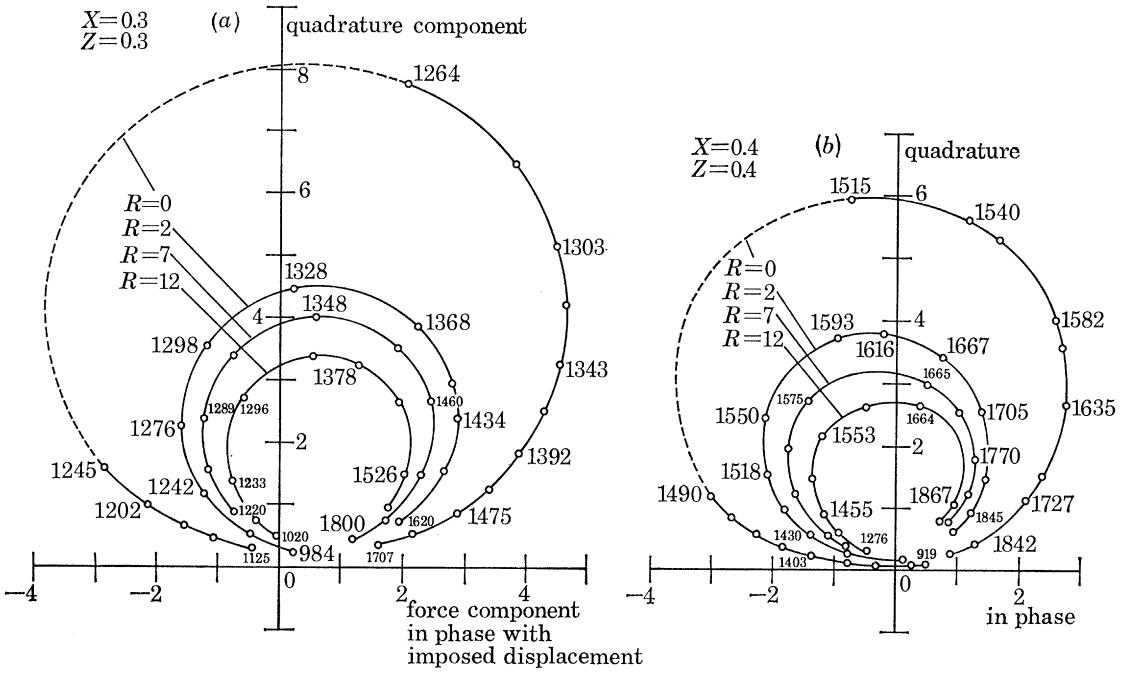

FIGURE 29. Force response loci for low velocities. Numbers on the curves are values of the frequency parameter f. For this tube, $\alpha = 1$; $\beta = 1.244$; $\gamma = 250$. Scale: 1 div. $= 89 \times 10^{-6}$ N.

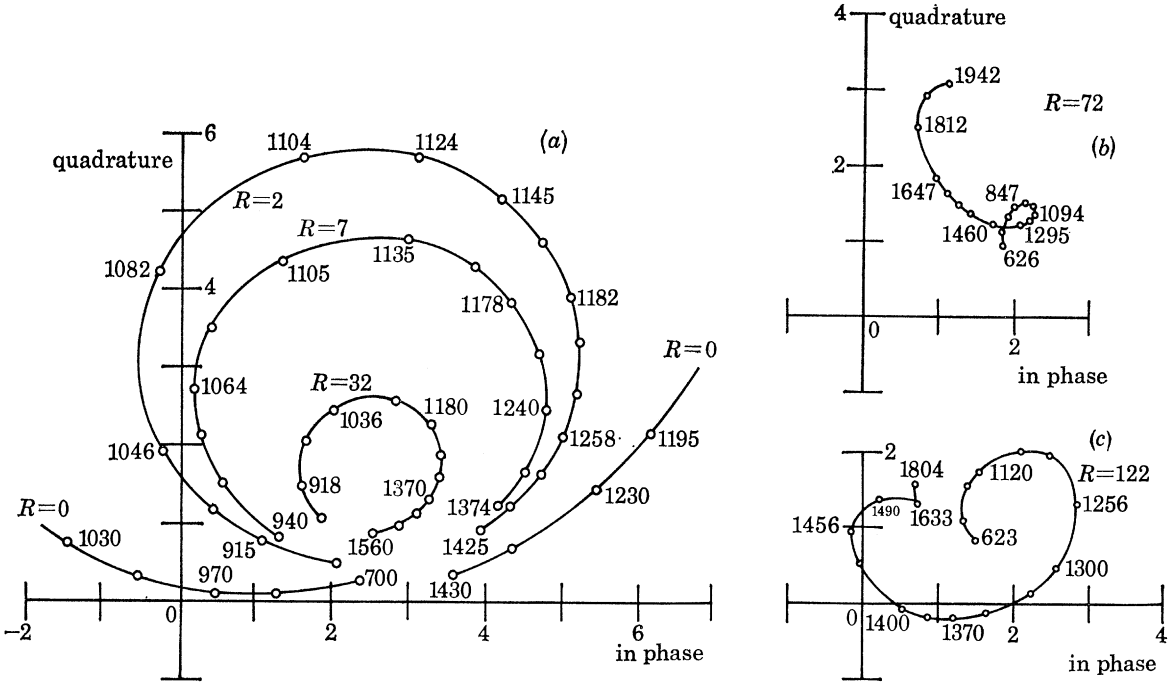

FIGURE 30. Force response loci for low velocities. Numbers on the curves are values of the frequency parameter f. For this tube, $\alpha = 1$; $\beta = 1.244$; $\gamma = 250$; $X = 0.15 = Z$. Scale: 1 div. $= 89 \times 10^{-6}$ N.

the phase difference between the force response vector and the displacement vector being measured from the positive real axis in the counterclockwise direction. This is in accordance with usual practice in plotting receptances for which the displacement response is plotted under the real axis when the system is excited by a harmonic force.

The two figures, 29 (*a*) and (*b*), show that each locus follows a circular arc progressing in a clockwise sense as the frequency increases. This conforms with the theoretical calculations presented before.

The resonance frequency of the tube is that frequency at which the force response reaches its minimum value. This is the frequency at the nearest point on the locus to the origin. The force response increases with increase of frequency until it reaches a maximum value; then it decreases again as the locus returns towards the origin, the frequency then approaching the second resonance frequency of the tube.

When the amplitude of the force response was near its maximum value, it was noted that the lower part of the tube oscillated violently. The excitation frequency when the force response was a maximum fell very close to the first natural frequency of the lower part of the tube as a pinned-free beam. This suggested that the excitation point acted as a hinge supporting the lower part and hence the reactive force at the 'hinge' was extremely large. In other words the harmonically excited clamped-free tube was composed of two subsystems joined together at the excitation point. These subsystems are the upper part behaving as a clamped-pinned tube and the lower part behaving as a pinned-free beam. The possibility of this 'dynamic interference' was anticipated in the theoretical analysis.

An interesting difference may be seen between the loci of figures 29 (*a*) and (*b*). While the frequency of the minimum force response is fairly constant ($f \approx 1000$ for all loci) the frequency of maximum force response increases considerably (f being from about 1260 to 1360 when $Z = 0.3$ and from about 1515 to 1614 when $Z = 0.4$). This is understandable since a larger value of Z means that the lower part is shorter and consequently possesses a higher natural frequency.

8.3. *Force response for low velocities*

Figures 30 (*a*)–(*c*) show the force response loci at a series of small water velocities. These loci all relate to the condition $X = 0.15 = Z$. Taking just the first of them, it can be seen that the resonance frequency of the tube, as indicated by the minimum force response, decreases with increase of velocity, while the phase angle increases to a maximum and then decreases again. These changes are to be expected on account of the increasing hydrodynamic damping that is associated with water velocity. This is easily seen when the curve for $R = 0$ is compared with that for $R = 2$. The resonance frequency varies only slightly whereas the phase angle varies considerably. Moreover, the minimum force response at resonance increases with water velocity, as one would expect since damping usually reduces the displacement response of a force excited system.

As the velocity is increased and the system approaches the instability boundary, the circular loop whose main contributor is the first natural mode of vibration diminishes gradually. This may be seen in figure 30 (*b*). At the same time another loop starts to form. This latter expands while the first loop nearly vanishes as the velocity is further increased, as may be seen in figure 30 (*c*). The main contributor to this new loop is the second mode of vibration of the tube – the unstable mode. Inflation of the loop is most pronounced near the origin of the complex plane especially near the critical velocity.

PHILOSOPHICAL TRANSACTIONS OF THE ROYAL SOCIETY A MATHEMATICAL, PHYSICAL & ENGINEERING SCIENCES

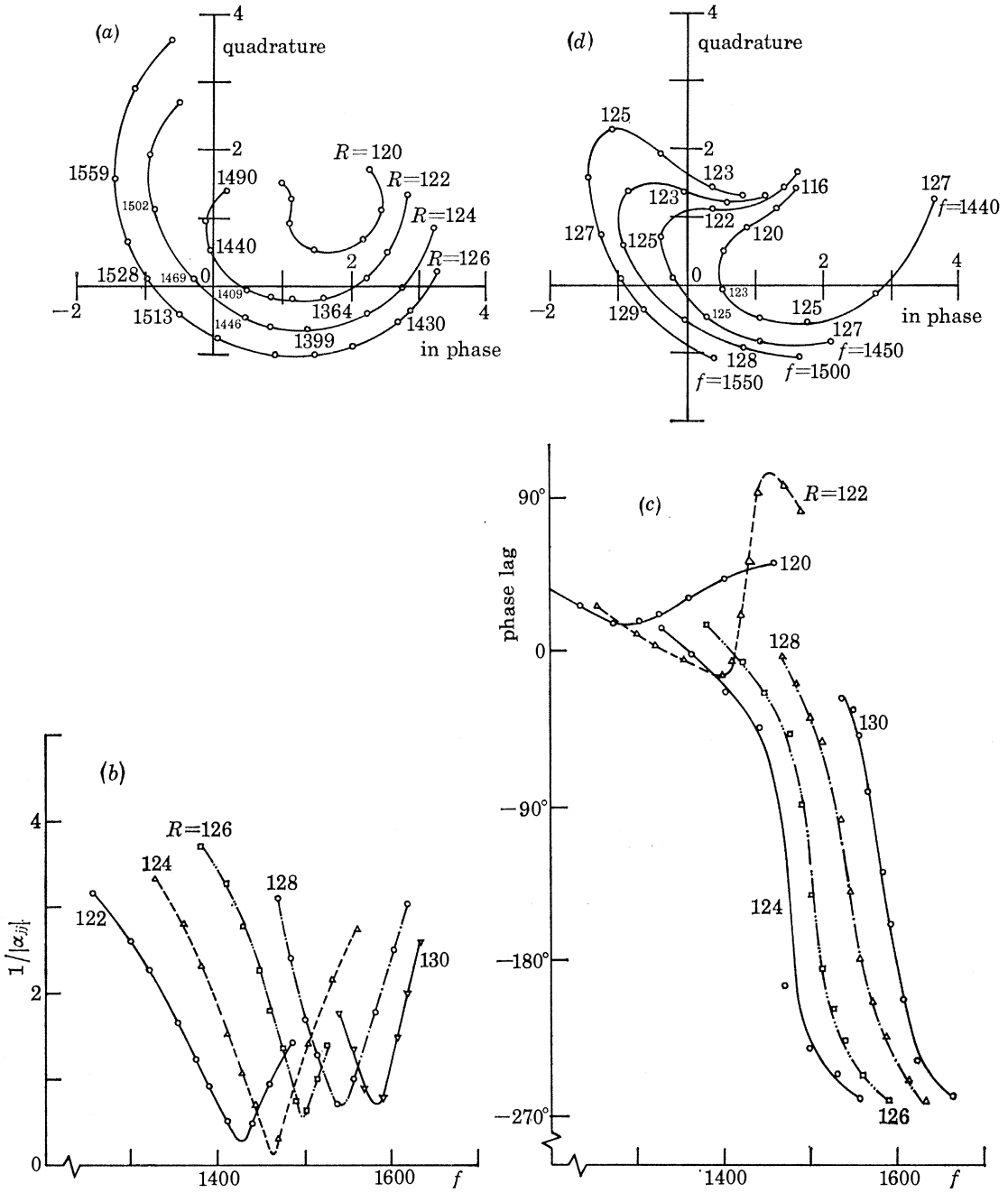

FIGURE 31. Variation of inverse receptance at the instability boundary. For this system: $\alpha = 1$; $\beta = 1.244$; $\gamma = 250$; $X = 0.15 = Z$. Scale in figures (a) and (d): 1 div. $= 44 \times 10^{-3}$ N/m. Numbers on the curves (a) are values of frequency parameter f, and on curves (d) are values of velocity parameter R.

PHILOSOPHICAL TRANSACTIONS OF THE ROYAL SOCIETY A MATHEMATICAL, PHYSICAL & ENGINEERING SCIENCES

The responses at the sections $X = 0.3$ and $X = 0.4$ exhibited the same features as those shown in figure 30.

8.4. *Harmonic force response at the instability boundary*

Figure 31 (*a*) shows the force response loci at the instability boundary. It confirms the theoretical prediction that the inverse receptance locus passes through the origin of the plane at the critical frequency. The shift of the curve across the origin from the side of increasing phase to the side of decreasing phase is very noticeable. It is believed that this is the first time such a diagram has been found experimentally for an unstable mechanical system.

The amplitude and phase of the force response are plotted against frequency in figures 31 (*b*) and (*c*) respectively. The minimum force response at the resonance frequency (sometimes called the residual force) decreases as the system approaches its instability boundary until it vanishes at the critical values of velocity and frequency. The effect of any parameter on the stability of the system can therefore be studied by investigating its effect on the residual force.

The change of the phase angle in figure 31 (*c*) is best understood by considering two different conditions. Before the instability boundary is reached the loci of the force response are to be found in the first quadrant and the phase angle increases continuously in the range between 0° and 90°. After the instability boundary has been reached the loci are confined generally in the other three quadrants and the phase angle decreases continuously from 0° to −270° via −90° and −180°.

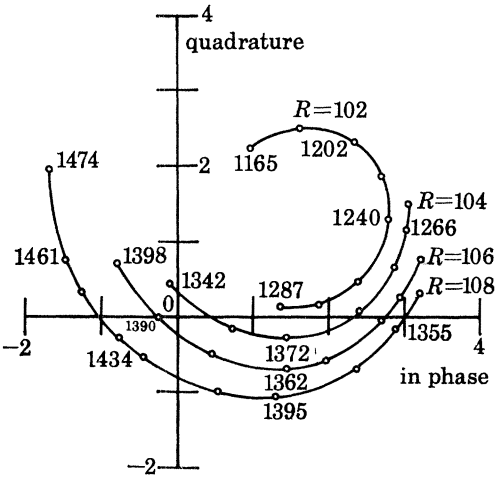

FIGURE 32. Inverse receptance at the instability boundary for a system in which $\alpha = 1.27$; $\beta = 1.244$; $\gamma = 250$; $X = 0.15 = Z$. Numbers on the curves are values of frequency parameter f. Scale: 1 div. = 44×10^{-3} N/m.

Figure 31 (*d*) shows the force loci near instability for constant frequencies, with the flow velocity varying along the curves. These loci were obtained independently by fixing the excitation frequency and changing the water velocity gradually. Gradual increase of water velocity at constant frequency produces similar loci to those resulting from gradual increase of frequency at constant velocity. Figures 31 (*a*) and (*d*) determine the instability boundary completely. The first gives bounds for the critical velocity according to the position of the origin of the complex plane among the loci. The second figure gives bounds for the critical frequency in a similar way. These bounds could be made as close as is desired merely by decreasing the increments of velocity and frequency.

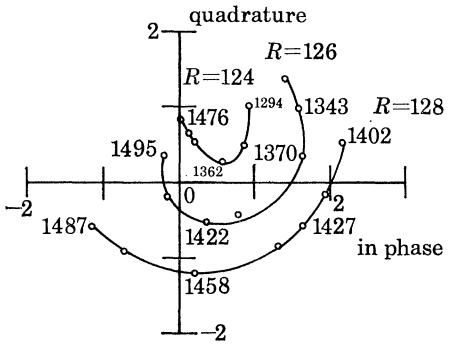

FIGURE 33. Inverse receptance at the instability boundary for a system in which $\alpha = 1.0$; $\beta = 1.244$; $\gamma = 250$; $X = 0.3 = Z$. Numbers on the curves are values of frequency parameter f. Scale: 1 div. = 44×10^{-3} N/m.

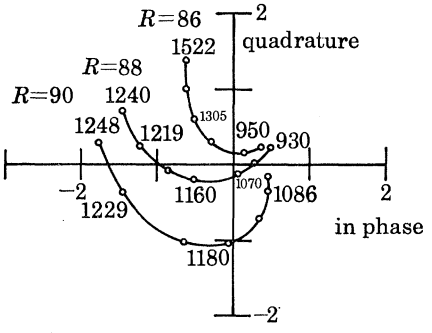

FIGURE 34. Inverse receptance at the instability boundary for a system in which $\alpha = 1.5$; $\beta = 1.244$; $\gamma = 250$; $X = 0.3 = Z$. Numbers on the curves are values of frequency parameter f. Scale: 1 div. = 44×10^{-3} N/m.

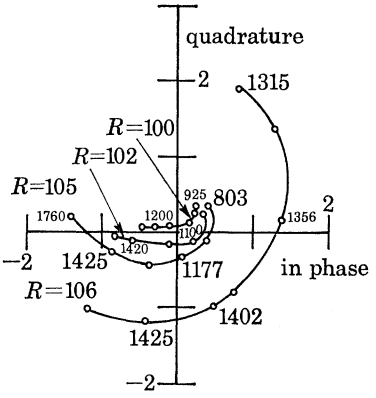

FIGURE 35. Inverse receptance at the instability boundary for a system in which $\alpha = 1.27$; $\beta = 1.244$; $\gamma = 250$; $X = 0.4 = Z$. Numbers on the curves are values of frequency parameter f. Scale: 1 div. = 44×10^{-3} N/m.

In the remaining figures only the frequency locus is plotted. This gives the critical velocity. The critical frequency is determined from the graph of force amplitude against frequency by interpolation between the frequencies at the velocity bounds. Figures 32–35 show the results of experiments carried out using different nozzles and different excitation points, as indicated by the values of α and (X, Z).

9. Conclusions

(i) Free oscillation of a vertical flexible tube conveying a fluid has been studied theoretically. The stability of the system has been examined, with particular reference to the nozzle parameter α, the gravity parameter γ and the damping present.

(ii) An analysis has been made of the direct receptance and its inverse for this non-conservative mechanical system. A vertical clamped-free tube conveying fluid has been investigated below, at and beyond its instability boundary. In particular, a method of determining the instability boundary of a non-conservative system has been examined, namely that of measuring, or plotting, the inverse receptance in a way similar to the application of the Nyquist criterion with automatic control systems.

The analysis revealed a phenomenon that may be termed 'dynamic interference'. The special features of the receptances of the clamped-free tube which are explained in terms of the properties of the clamped-pinned tube suggest that, without an understanding of the dynamic interference, the results are open to misinterpretation.

(iii) Free vibration has been examined experimentally. The assumption of small Kelvin damping within the structure appears to bridge the gap between a theory which admits only hydrodynamic damping and the experimental results, and to do so very well indeed. In particular, the complicated interdependence of the follower force, the weight load and the Kelvin damping (i.e. of the parameters α, γ and κ) has been elucidated theoretically and verified experimentally.

The static distortion phenomenon reported here may turn out to have a wider importance. It might shed some light on the neutral equilibrium of a cantilever with a follower force, where static analysis fails.

(iv) In experiments on forced vibration the applicability has been examined of resonance testing techniques near an instability boundary. Curves plotted for different values of parameters near the instability boundary confirm the reliability and consistency of the harmonic force response method in an investigation of mechanical stability. Care must be taken, however, to avoid (or properly to interpret) 'dynamic interference' between the subsystems that are identified by the excitation process. Examples of this with the vertical tube were provided by resonance of its lower part and divergence of its upper part. In practice, dynamic interference could so obscure results as to lead to erroneous conclusions.

No allowance was made for damping, either external or internal, in the theory presented for forced vibration. We therefore cannot compare the theoretical predictions directly with the experimental results. Nevertheless it was easy to measure the critical velocity and the critical frequency of the tube in free vibration and the values found compared very well with the force response results.

PHILOSOPHICAL TRANSACTIONS OF THE ROYAL SOCIETY A MATHEMATICAL, PHYSICAL & ENGINEERING SCIENCES

10. Appendix. Root locus diagram of the clamped-pinned tube

Analysis of free vibration of the clamped-pinned tube is performed in the same way as it is for the clamped-free tube. The equation of motion is

$$\boldsymbol{I}\ddot{\boldsymbol{P}} + \mu\beta\bar{\boldsymbol{E}}\dot{\boldsymbol{P}} + [\bar{\boldsymbol{A}} + \mu^2\alpha\bar{\boldsymbol{G}} + \gamma\bar{\boldsymbol{H}}]\,\boldsymbol{P} = \boldsymbol{0}. \tag{A 1}$$

The elements of the matrices $\bar{\boldsymbol{E}}$, $\bar{\boldsymbol{A}}$, $\bar{\boldsymbol{G}}$ and $\bar{\boldsymbol{H}}$ are determined by integrations similar to those in equations (42) but with the characteristic functions of a clamped-pinned beam obeying the appropriate end conditions. Thus their elements are given by:

$$\left.\begin{aligned}
\bar{E}_{rs} &= \int_0^1 \Phi_r \Phi_s' \,\mathrm{d}X = \frac{1}{\lambda_r^4 - \lambda_s^4}[(\Phi_r''' \Phi_s' - \Phi_r' \Phi_s''')_l + (\Phi_r'' \Phi_s'')_0] \\
\bar{E}_{rr} &= \int_0^1 \Phi_r \Phi_r' \,\mathrm{d}X = 0 \\
\bar{A}_{rs} &= \int_0^1 \Phi_r \Phi_s^{\mathrm{iv}} \,\mathrm{d}X = 0 \\
\bar{A}_{rr} &= \int_0^1 \Phi_r \Phi_r^{\mathrm{iv}} \,\mathrm{d}X = \lambda_r^4 \\
\bar{G}_{rs} &= \int_0^1 \Phi_r \Phi_s'' \,\mathrm{d}X = \frac{1}{\lambda_r^4 - \lambda_s^4}[(\Phi_r'' \Phi_s''' - \Phi_r''' \Phi_s'')_0] \\
\bar{G}_{rr} &= \int_0^1 \Phi_r \Phi_r'' \,\mathrm{d}X = \sigma_r \lambda_r - \sigma_r^2 \lambda_r^2 \\
\bar{H}_{rs} &= \int_0^1 [(X-1)\,\Phi_r \Phi_s'' + \Phi_r \Phi_s'] \,\mathrm{d}X = \frac{1}{\lambda_r^4 - \lambda_s^4}[(3 + C_{rs})\,(\Phi_r' \Phi_s''')_l + (2 + C_{rs})\,(\Phi_r'' \Phi_s'')_0 \\
&\quad + (1 + C_{rs})\,(\Phi_r''' \Phi_s')_l - (\Phi_r'' \Phi_s''' - \Phi_r''' \Phi_s'')_0] \quad \text{where} \quad C_{rs} = \frac{4}{(\lambda_r/\lambda_s)^4 - 1} \\
\bar{H}_{rr} &= \int_0^1 [(X-1)\,\Phi_r \Phi_r'' + \Phi_r \Phi_r'] \,\mathrm{d}X = \tfrac{1}{2} - \sigma_r \lambda_r + \tfrac{1}{2}\sigma_r^2 \lambda_r^2.
\end{aligned}\right\} \tag{A 2}$$

Values of λ_r and σ_r here are those of the clamped-pinned beam.

The steps in the solution of equation (A 1) are exactly the same as those explained for the clamped-free tube and the root locus diagram is shown in figure 18. This diagram is drawn for the values $\alpha = 3$, $\beta = 0.9$ and $\gamma = 5$. It is based on a four mode analysis, so that $n = 4$. The four branches all coincide with the imaginary axis until they reach the origin. Numbers going along the branches indicate values of the velocity parameter μ.

The authors wish to acknowledge the help they have received from Dr A. Simpson, who drew their attention to the approach discussed in § 1.2.

References

Ashley, H. & Haviland, G. 1950 Bending vibrations of a pipe line containing flowing fluid. *J. Appl. Mech., Trans. Amer. Soc. mech. Engrs.* **72**, 229–232.

Benjamin, T. B. 1961 Dynamics of a system of articulated pipes conveying fluid, I and II. *Proc. R. Soc. Lond.* A **261**, 457–499.

Bishop, R. E. D. & Gladwell, G. M. L. 1963 An investigation into the theory of resonance testing. *Phil. Trans. R. Soc. Lond.* A **255**, 241–280.

Bishop, R. E. D. & Johnson, D. C. 1960 *The mechanics of vibration.* Cambridge University Press.

Bolotin, V. V. 1964 *Dynamic stability of elastic systems*. London: Holden Day.
Brann, R. P. 1965 The stability of vehicles having coned wheels. Ph.D. Thesis, University of London.
Brann, R. P. 1967 Notes on the harmonic excitation of multidegree unstable systems. *J. Sound Vib.* **5**, 81–92.
Duncan, W. J., Thom, A. S. & Young, A. D. 1960 *The mechanics of fluids*, p. 131. London: Edward Arnold.
Frazer, R. A. 1939 On the power input required to maintain forced oscillations of an aeroplane wing in flight. *R and M. No.* 1872, *Tech. Rept. Aero Res. Comm.*, **2**, 687–704.
Frazer, R. A. & Jones, W. P. 1937 Forced oscillations of aeroplanes with special reference to von Schlippe's method of predicting critical speeds for flutter. *R and M. No.* 1795, *Tech. Rept. Aero. Res. Comm.*, **1**, 445–470.
Gregory, R. W. & Paidoussis, M. P. 1966 Unstable oscillations of tubular cantilevers conveying fluid. II. Experiments. *Proc. R. Soc. Lond.* A **293**, 528–542.
Kennedy, C. C. & Pancu, C. D. P. 1947 Use of vectors in vibration measurements and analysis. *J. Aero. Sci.* **14**, 603–625.
Muhlstein, L. 1966 A forced vibration technique for investigation of panel flutter. AIAA Paper No. 66-769, AIAA Aerodynamic Testing Conference, Los Angeles.
Paidoussis, M. P. 1970 Dynamics of tubular cantilevers conveying fluid. *J. Mech. Eng. Sci.* **12**, 85–103.
Payne, A. R. & Scott, J. R. 1960 *Engineering design with rubber*. London: McLaren.
von Schlippe, B. 1936 Zur Frage der Selbsterregten Flügelschwingungen (Ermittlung der Kristischen Geschwindigkeit durch Flugschwingungsversuche) *Luftfahrtschung*, Bd. 13, Nr. 2.
Wahed, I. F. A. 1969 Dynamic instability of hanging flexible tubes conveying fluid at high speed. Ph.D. Thesis, London University.

PHILOSOPHICAL TRANSACTIONS OF THE ROYAL SOCIETY A MATHEMATICAL, PHYSICAL & ENGINEERING SCIENCES

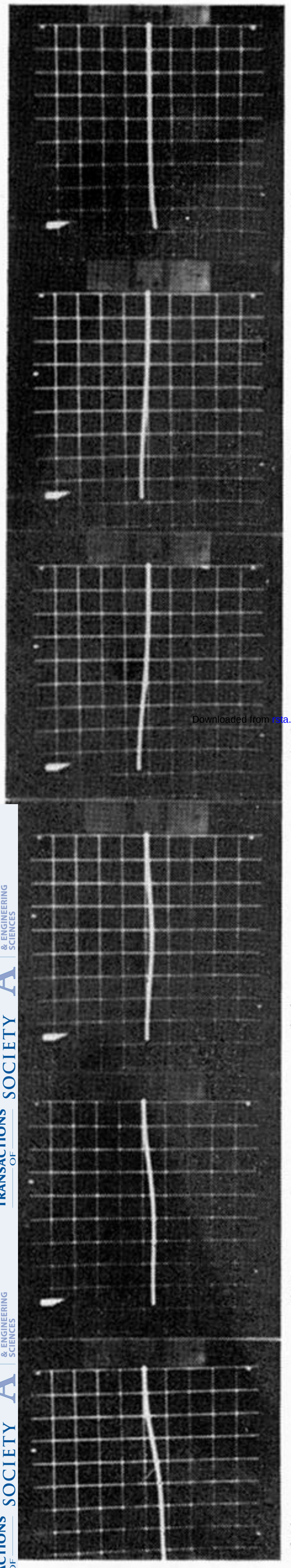

A ($\mu=0$)

B

C

D

E

F($\mu<\mu_c$)

FIGURE 22.

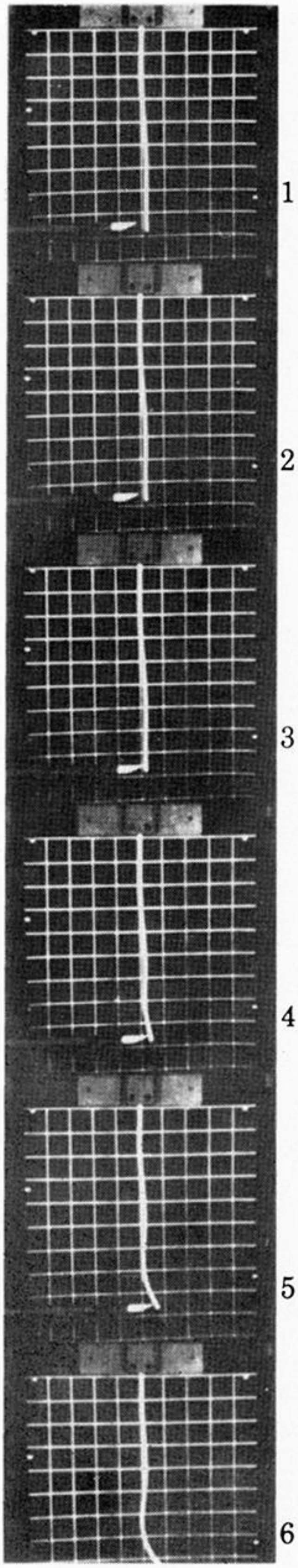

1

2

3

4

5

6

FIGURE 23.

FIGURE 22. Static distortion shapes before instability.

FIGURE 23. Dynamic instability after touching the free end of the tube.